To the Graduate Council:
I am submitting herewith a thesis written by Brett Eugene Brady entitled "Low-Cost Image Collection and Compilation for Enhanced In-Situ Monitoring in Laser-Powder Bed Fusion." I have examined the final paper copy of this thesis for form and content and recommend that it be accepted in partial fulfillment of the requirements for the degree of Master of Science, with a major in Aerospace Engineering.

_____

Dr. Bradley Jared, Major Professor

We have read this thesis
and recommend its acceptance:

_____

Dr. Bradley Jared

_____

Dr. Sudarsanam Babu

_____

Dr. Subhadeep Chakraborty

Accepted for the Council:

_____

Dixie L. Thompson

Vice Provost and Dean of the Graduate School

To the Graduate Council:
I am submitting herewith a thesis written by Brett Eugene Brady entitled "Low-Cost Image Collection and Compilation for Enhanced In-Situ Monitoring in Laser-Powder Bed Fusion." I have examined the final electronic copy of this thesis for form and content and recommend that it be accepted in partial fulfillment of the requirements for the degree of Master of Science, with a major in Aerospace Engineering.

Dr. Bradley Jared, Major Professor

We have read this thesis
and recommend its acceptance:

Dr. Bradley Jared

Dr. Sudarsanam Babu

Dr. Subhadeep Chakraborty

Accepted for the Council:

Dixie L. Thompson

Vice Provost and Dean of the Graduate School

(Original signatures are on file with official student records.)

Low-Cost Image Collection and Compilation for Enhanced In-Situ Monitoring in Laser-Powder Bed Fusion

A Thesis Presented for the

Master of Science

Degree

The University of Tennessee, Knoxville

Brett Eugene Brady

August 2024

© by Brett Eugene Brady, 2024
All Rights Reserved.

Acknowledgements

I would like to thank first and foremost my parents, who always pushed me to find my limits and exceed them. I would like to thank my research group who helped me immensely in this research.

I would also like to acknowledge support from the Air Force Small Business Technology (STTR) contract FA2394-23-C-B021 for funding the work herein.

"To give anything less than your best, is to sacrifice the gift." - Steve Prefontaine

Abstract

Laser-Powder Bed Fusion (L-PBF) additive manufacturing relies on precise control for quality assurance and reproducibility, necessitating advanced in-situ monitoring techniques. Presented is a novel low-cost approach to image collection and compilation to enable in-situ monitoring in L-PBF in ways not performed to date, i.e., at a lower cost. The research incorporates optical, near-infrared (NIR), and infrared (IR) imaging modalities to record and, in the future, analyze and detect defects during the L-PBF process. Off-axis cameras with different spectral sensitivities complicates the comparison of images due to differing image planes. A low-cost, calibration plate is used to create common image planes through perspective transforms that allows the overlay of images from differing cameras and camera orientations, a prerequisite to achieving defect detection. This calibration plate uses two materials with differing emissivity to allow calibration across differing modalities. This approach results in a maximum image error of only 1 mm. Data is collected using a custom, Python-based recording script, optimized for real-time monitoring and storage using the HDF5 file format. The findings suggest that this low-cost solution can be effectively implemented, providing the base work for future work in defect detection.

Table of Contents

1 In-Situ Monitoring for Laser-Powder Bed Fusion **1**

1.1 Introduction 1

1.2 Need for in-situ monitoring 2

1.3 Prior work in-situ monitoring 2

1.3.1 Optical 2

1.3.2 Near-Infrared 3

1.3.3 Infrared 3

1.4 Prior work in Calibration Plates for Perspective Correction 5

1.5 Prior work in L-PBF image acquisition 5

2 Experimental Setup **10**

2.1 Hardware Setup 10

2.1.1 Laser-Powder Bed Fusion Platform 10

2.1.2 Camera Hardware 12

2.1.3 Image Acquisition Software 13

2.2 Comparison to Current Software 15

2.2.1 Computer Hardware 16

3 Data Collection and Storage **17**

3.1 Data Collection 17

3.1.1 Sequential Recording 17

3.1.2 Experiment outline for finalizing DAQ 18

3.1.3 Multiprocessing Recording 18
3.1.4 Separate Console Scripts 22
3.1.5 Threaded Recording 22
3.1.6 Optimized Recording Process 26
3.2 Data Collected 30
3.2.1 Optical 30
3.2.2 NIR 30
3.2.3 FLIR 33
3.3 Data Storage 36
3.3.1 HDF5 Format 36
3.3.2 Compression 37
3.3.3 Optical Data Storage 37
3.3.4 Long Term Storage 37

4 Calibration Plate and Perspective Correction 38
4.1 Objective 38
4.2 Calibration Plate 38
4.3 Data Collection 40
4.3.1 Hardware Used 40
4.3.2 Pinhole Camera Model 41
4.3.3 Calibration Process 45
4.4 Results and Discussion 47
4.4.1 Initial Findings 47
4.4.2 Perspective Correction Results 62

5 Data Utilization 66
5.1 Computer Hardware 66
5.2 Post-Build Data Processing 66
5.2.1 Optical Processing 66
5.2.2 NIR Processing 67

5.2.3 IR Processing 67

6 Conclusions **76**

Bibliography **78**

A Farsoon FS271M Nominal Settings **87**

Vita **91**

List of Tables

1.1 Summary of thermal cameras used for previous research. 9

List of Figures

1.1 Spectral response for Pixelink PL-D734MU family of cameras (Pixelink, 2024b). 8

2.1 Farsoon FS271M L-PBF machine located in the MakerLab at the University of Tennessee. 11
2.2 Addiguru optical monitoring system. 14

3.1 Standard laser pattern supplied by Farsoon software. 19
3.2 Multiprocessing layerwise image showing dropped frames. 20
3.3 Multiprocessing timeline showing event timing during image acquisition. 21
3.4 Separate script layerwise image showing reduced dropped frames. . . 23
3.5 Separate script timeline showing event timing during image acquisition. 24
3.6 Threading script layerwise image. 27
3.7 Threading script event timeline during image acquisition. 28
3.8 Data acquisition process flow. 29
3.9 Visual representation of 'numpy.max' algorithm. 32
3.10 Example of data gaps due to FOT. A layerwise NIR image of a circular part from layer 234 reveals line gaps that interrupt the full circular silhouette. These gaps indicate areas where data could not be collected during the frame overhead time. 34
3.11 FOT in 5% increments of the max width and height to 50% of the max width and height. 35

4.1 Manufactured Calibration Plate with 155 mm ruler for scale. 39
4.2 Pinhole camera model (Bradski, 2000). 42
4.3 Flowchart for perspective transform of images. 46
4.4 Uncorrected NIR image of calibration plate within the FS271M build chamber. 48
4.5 Overlayed images of detected of NIR corrected pattern (red) to mathematical-based model of the plate (green). 49
4.6 NIR image center location difference vector field in pixels (scaled by 10). 50
4.7 Histogram of error magnitudes for NIR. 51
4.8 Reprojection error of corrected NIR image. 52
4.9 Uncorrected FLIR image of calibration plate within the FS271M build chamber. 54
4.10 Overlayed images of detected of FLIR corrected pattern (red) to mathematical-based model of the plate (green). 55
4.11 FLIR image center location difference vector field plot in pixels (scaled by 1000). 56
4.12 Histogram of error magnitudes for FLIR. 57
4.13 Reprojection error of corrected FLIR image. 58
4.14 Uncorrected optical image of calibration plate within the FS271M build chamber. 59
4.15 Overlayed images of detected optical corrected pattern (red) to mathematical-based model of the plate (green). 60
4.16 Optical image center location difference vector field plot in pixels (scaled by 10). 61
4.17 Distribution of error magnitudes for optical. 63
4.18 Reprojection error of corrected optical image. 64
4.19 Final corrected images after perspective correction 65

5.1 Optical saliency maps showing potential areas of interest. 69

5.2 Example of pre-powder optical image. 70
5.3 Example of post-powder optical image. 71
5.4 Example of layer-wise NIR image. 72
5.5 Example of IR interpass temperature. 73
5.6 Example of IR temporal temperature gradient °C/s. 74
5.7 Example of IR spatial temperature gradient °C/pixel 75

Nomenclature

API	Application Programming Interface
CNN	Convolutional Neural Network
DAQ	Data Acquisition
FLIR	Forward-Looking Infrared
FOT	Frame Overhead Time
fps	Frames Per Second
GB	Gigabyte
GPU	Graphics Processing Unit
GUI	Graphical User Interface
HDF5	Hierarchical Data Format version 5
IR	Infrared
L-PBF	Laser-Powder Bed Fusion
LVDS	Low Voltage Differential Signaling
MB	Megabyte
MHz	Megahertz

MP	Megapixel
NIR	Near-Infrared
PVC	Polyvinyl Chloride
RAM	Random Access Memory
ROI	Region of Interest

Chapter 1

In-Situ Monitoring for Laser-Powder Bed Fusion

1.1 Introduction

Laser-powder bed fusion (L-PBF) is an additive manufacturing technique that uses a laser to selectively melt and fuse metallic powders, such as titanium or stainless steel, to create complex geometries layer by layer. This process offers significant advantages in terms of design flexibility, material efficiency, manufacturing speed, and the ability to produce parts with internal structures that are difficult or even impossible to achieve with traditional subtractive-based manufacturing methods. Additively manufactured parts are highly susceptible to material and part defects developed during printing. The precision and quality assurance of L-PBF processes are critical for ensuring the mechanical properties and reliability of the printed parts. Process monitoring in the L-PBF process can detect defects such as porosity and dimensional inaccuracies, which are essential for applications in aerospace, medical, and other high-performance industries.

1.2 Need for in-situ monitoring

In-situ monitoring refers to the real-time observation and analysis of the manufacturing process as it occurs. This can be accomplished in many different observation modalities such as cameras, temperature measurements, or even acoustic-based data. In the context of L-PBF, in-situ monitoring allows for the detection of defects and anomalies during the build process through algorithms, enabling immediate corrective actions, identification of parts that do not meet specifications, or process termination to ensure higher-quality end products. The benefits of in-situ monitoring include enhanced process control, reduced waste, improved repeatability, and the ability to meet stringent industry standards. However, several challenges persist in effectively monitoring L-PBF processes. These include the need for different cameras and camera angles to capture all aspects of the build, managing long print durations that can span several hours, and integrating various types of monitoring equipment within the constrained physical dimensions of an L-PBF machine. Previous research has shown that in-situ is capable of identifying these defects with expensive, high bandwidth, high-resolution sensors.

1.3 Prior work in-situ monitoring

Various wavelengths can give information about what possible defects may occur in a printed part. By analyzing differing sections of the electromagnetic spectrum, insights into a range of defects from porosity and warpage to spatter and geometric inaccuracies. These defects can lead to part failure, so understanding where these defects occur and why are critical in manufacturing parts that meet specifications.

1.3.1 Optical

Optical light can cover a wavelength range of 380-750 nm. Researchers have shown that, in combination with neural networks, optical imaging can reliably detect

porosity (Nguyen et al., 2023), overheating (Nguyen et al., 2023), warpage (Nguyen et al., 2023; Scime and Beuth, 2018; Xiao et al., 2020), recoater effects (Scime and Beuth, 2018), debris (Scime and Beuth, 2018), distortion (Land et al., 2015), geometric integrity (Gaikwad et al., 2019), part shifting (Xiao et al., 2020), and powder short feed (Xiao et al., 2020).

Addiguru

The main project collaborator's is Addiguru. Addiguru's proprietary optical monitoring software is used for this research. Addiguru is used for optical observation and can detect optical defects such as powder bed anomalies, part elevation, spatter, recoater streaking, and recoater hopping in real time. This is accomplished using computer vision algorithms and convolution neural networks (CNN) (Addiguru, 2024).

1.3.2 Near-Infrared

The near-infrared (NIR) spectrum covers wavelengths of light from 750 to 1.4 mm. Researchers have shown that NIR imaging can be correlated to porosity present within the finished part (Yoder et al., 2019). It has also been shown that NIR images can be correlated to part failures (Craeghs et al., 2012). Spatter detection can also be generated by NIR imaging. This spatter detection leads to spatter-induced stochastic lack of fusion (Schwerz et al., 2021; Snow et al., 2023a). Notably, researchers have highlighted that not all bright spots in NIR data correspond to subsurface flaws, and vice versa (Snow et al., 2023b).

1.3.3 Infrared

The infrared (IR) spectrum covers light with wavelengths from 750nm to 1mm. Thermographic data can be derived using the information gathered in this spectrum. It has been shown that IR measurements can be used to determine the geometric

accuracy of the printed part in-situ(Doubenskaia et al., 2015; Mohr et al., 2020c; Elwarfalli, 2020). Researchers have also shown that cooling rates are critical in determining the micro structure (Alldredge et al., 2018; Mohr et al., 2020a) and that cooling rates are highly localized and can vary significantly within a single layer (Lane et al., 2016). It has also been shown that delamination defects can be identified with high accuracy utilizing thermographic data (Patel et al., 2020; Rieder et al., 2020). Another defect that has been widely identified through thermographic measurements is porosity (Lough et al., 2022; Gong et al., 2014; Gordon et al., 2020; King et al., 2014; Wang et al., 2021; Promoppatum et al., 2022; Mireles et al., 2015; Bartlett et al., 2018; Forien et al., 2020). Researchers have also shown that infrared measurements can gather meaningful information about the spatter and plume coming from the part. Spatter and plume formation can lead to defects in the final part through spatter (McNeil et al., 2020), surface irregularities (Khairallah et al., 2016; Gunenthiram et al., 2018), and inconsistencies in micro-structures (Gunenthiram et al., 2018).

Interpass Temperature

Interpass temperature has been shown by researchers to inform the presence of process defects as well. Interpass temperature is defined as the temperature of a previously deposited layer of material just before a new layer is deposited on top of it. A high interpass temperature can lead to reduced porosity, while a low interpass temperature can lead to increased porosity due to inadequate fusion (Williams et al., 2019).

Temperature Gradient

The temperature gradient, both spatially and temporal, can be used to detect and predict part defects. Researchers have shown that slow thermal decay can be correlated to large scale defects. Thermal decay has also been shown to be caused by changes in the local thermal conductivity, not preheat conditions from laser scan strategy and sectional geometry interactions. Spatial and temporal infrared signature

changes were also related to thermo-mechanical drivers of cracking, agreeing with the measured defect distribution. Due to the differing conditions of builds such as number of parts and size of the builds, qualifications must be performed on a build basis, highlighting the need for in-situ process monitoring for L-PBF (McNeil et al., 2020).

1.4 Prior work in Calibration Plates for Perspective Correction

Previous efforts in the field have attempted to address the challenges of in-situ monitoring of off-axis imaging with varying degrees of success. Methods such as those discussed by Usamentiaga (Usamentiaga et al., 2017) emphasize the need for varying materials in a calibration pattern and the potential need for a heating element for contrast in the IR spectrum. The work completed by ElSheikh (ElSheikh et al., 2023) has identified the superior performance of circular patterns when compared to square-based calibration patterns. This provides a good basis for the following work as it eliminates the need to test with square-based patterns. ElSheikh's previous work has also demonstrated the use of heating elements in many designs and recognized that their own calibration pattern manufacturing had been manufactured utilizing laser-based cutters.

1.5 Prior work in L-PBF image acquisition

Prior work in L-PBF data acquisition has largely been completed using high level proprietary software as well as high cost imaging sensors. This has been done for optical, NIR, and IR cameras.

Optical and near-infrared (NIR) spectral sensitivities often overlap, allowing a NIR image to be created from an optical camera using appropriate filters. By filtering

out visible light and isolating the NIR wavelengths, an optical camera sensor can capture NIR images. Many different researchers have used this fact (Yang et al., 2020; Vasileska et al., 2020b,a; Mohr et al., 2020c)

A dedicated NIR camera, however, will perform better due to its higher quantam efficiency allowing more light in a specific region of interest to be collected. NIR-specific sensors are designed to be more sensitive to NIR wavelengths, providing higher quality images, better contrast, and more accurate data compared to modified optical cameras.

Figure 1.1 shows the quantum efficiency of two different cameras, an optical (Pixelink PL-D734MU) and a NIR based camera (Pixelink PL-D734MU-NIR) which is the NIR camera used in this research. Quantum emission is an absolute measure of efficiency, showing the proportion of photons converted to electrons. For observing spectral emissions in the NIR, the spectrum of 700 to 1000 nm is the most noteworthy. Figure 1.1 clearly shows that the NIR camera is better than the optical in terms of quantum efficiency resulting in areas of almost a 25% difference in quantum efficiency within the NIR spectrum region of interest (750 - 900 nm).

Table 1.1 lists previous IR thermal cameras used by various researchers, the software that was used to record the images, the field of view (FOV), and the price estimate of the camera. Since most cameras do not have publicly listed prices, their costs are determined by contacting other researchers and comparing them with cameras of similar specifications. Most software used was Teledyne FLIR software that first records the video and then does limited processing on it. This processing is usually restrictive on what can be accomplished using the software. Data captured using these software are usually extracted and additional processing and analysis is completed post print.

FLIR cameras are renowned for their high performance and advanced features, particularly in thermal imaging. However, they come with a significant cost, often reaching tens of thousands of dollars and sometimes into the hundreds of thousands. This expense can be prohibitive for many applications, especially those requiring multiple units, commercialization, or are constrained by budget limitations. To address this, this research explores a low-cost alternative that can offer acceptable performance for specific applications – the FLIR A50.

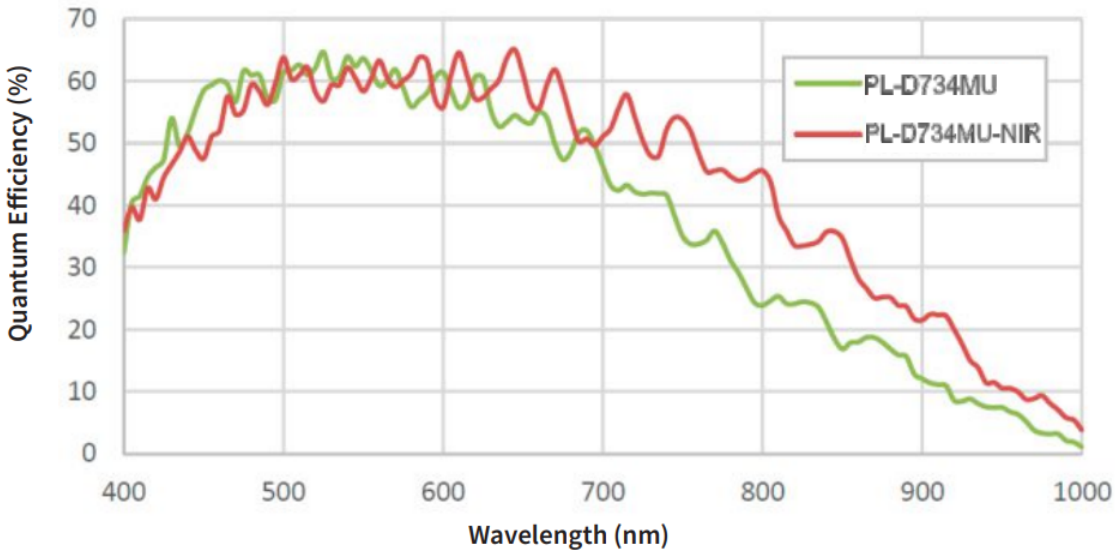


Figure 1.1: Spectral response for Pixelink PL-D734MU family of cameras (Pixelink, 2024b).

Table 1.1: Summary of thermal cameras used for previous research.

Reference	Company	Model	Software Used	FOV	Price (est.)
AbouelNour and Gupta (2023)	FLIR	E5-XT	FLIR Thermal Studio	160 x 120	$1,200
Ashby (2022)	FLIR	A6700sc	FLIR ResearchIR 4	640 x 512	$50,000
Baumgartl et al. (2020)	PYROVIEW	640G	Unknown	640 x 480	$20,000
Deckers et al. (2023)	FLIR	x6900sc	FLIR ResearchIR 4	640 x 512	$95,000
Estalaki et al. (2022)	FLIR	SC6201	Unknown	640 x 512	$65,000
Foster et al. (2018)	FLIR	SC8200	Custom MatLab	1024 x 1024	$80,000
Fournet-Fayard et al. (2023)	FLIR	x8500sc	FLIR ResearchIR	1280 x 1024	$100,000
Liu et al. (2022)	FLIR	A655sc	Unknown	640 x 480	$25,000
Lough et al. (2022)	FLIR	SC6201	Unknown	640 x 512	$65,000
Mohr et al. (2020b)	InfraTec	ImageIR8300	IRBIS3	640 x 512	$130,000
Plotnikov et al. (2019)	FLIR	A65	Unknown	640 x 512	$7,500
Raplee et al. (2017)	FLIR	7600	FLIR ResearchIR	640 x 512	$75,000
Raplee et al. (2020)	FLIR	SC8200	Unknown	1024 x 1024	$80,000
Ridwan et al. (2014)	FLIR	SC645	Custom Labview	640 x 480	$25,000
Scarpitti and Tocci (2021)	FLIR	x6901	FLIR ResearchIR	640 x 512	$90,000
Scime et al. (2020)	FLIR	A35	Unknown	320 x 256	$3,000
Yakout et al. (2021)	InfraTec	ImageIR8300	IRBIS3	640 x 512	$130,000

Chapter 2

Experimental Setup

2.1 Hardware Setup

2.1.1 Laser-Powder Bed Fusion Platform

The L-PBF used in this research is the Farsoon FS271M, located in the MakerLab at the University of Tennessee, Knoxville seen in Figure 2.1. The Farsoon FS271M is manufactured by Farsoon Technologies. The external dimensions of the machine are 1750 x 1430 x 1860 mm and it has a build envelope of 275 x 275 x 340 mm. It is capable of a layer thickness of 0.02 to 0.1 mm and has a max scanning speed of 15.2 m/s. The Farsoon FS271M uses a single 500W fiber laser with a high-precision three-axis digital galvo system with a focused beam diameter at the build plate plane of approximately 70 μm. It is capable of using either Argon or Nitrogen for inert gas shielding with an average inert gas consumption rate in the process of less than 3 L/min (Farsoon-Technologies, 2020). Stainless Steel 316L powder is currently used in the machine. Nominal settings used for experiments can be found in Appendix A.



Figure 2.1: Farsoon FS271M L-PBF machine located in the MakerLab at the University of Tennessee.

2.1.2 Camera Hardware

Optical

The optical camera used for data collection for this experiment is the Basler acA5472-17um. This camera utilizes a Sony IMX183 CMOS sensor, delivering 17 frames per second (fps) and using USB 3.0 digital interface. The camera provides a 20.0 megapixel (MP) image that is 5472 x 3648 pixels. Images are captured in a mono grayscale format and can have a pixel depth of both 10 bits and 12 bits. The Basler acA5472-17um retails for $729.00 (Basler, 2024).

Near-Infrared

Images in the NIR spectrum are captured using the Pixelink PL-D734MU-NIR-T camera. The PL-D734MU-NIR-T is a USB 3.0 camera that utilizes a 4.2 MP CMOSIS CMV 4000 sensor with a global shutter to deliver images of size 2048 x 2048 pixels at a maximum frame rate of 90.3 fps. A global shutter captures an image py exposing all pixels simultaneously, eliminating motion artifacts associated with rolling shutter that occur when imaging fast-moving objects. The camera is capable of delivering images in both 8-bit and 10-bit formats. The camera is capable of an exposure time from 28 μs to 5 seconds. This sensor is paired with a Kowa LM16HC lens as well as a bandpass filter and ND filter. This setup retails at approximately $2,200 (Pixelink, 2024b).

Infrared

The infrared spectrum is captured utilizing the FLIR A50 Smart Sensor. The FLIR A50 is capable of capturing images at up to 30 fps. It is capable of capturing both optical and radiometric images with the resolution of 1280 x 960 pixels and 464 x 348 pixels, respectively. Thermal images are captured with a dynamic range of 16 bits. The FLIR A50 is capable of thermal sensitivity of less than 35 mK and an accuracy of $\pm 2^{\circ}$C. The camera supports multiple industrial protocols including EtherNet/IP,

Modbus TCP, and MQTT. It is used in this research via the EtherNet/GigE connection. The FLIR A50 retails at $6,950 (FLIR, 2024a).

2.1.3 Image Acquisition Software

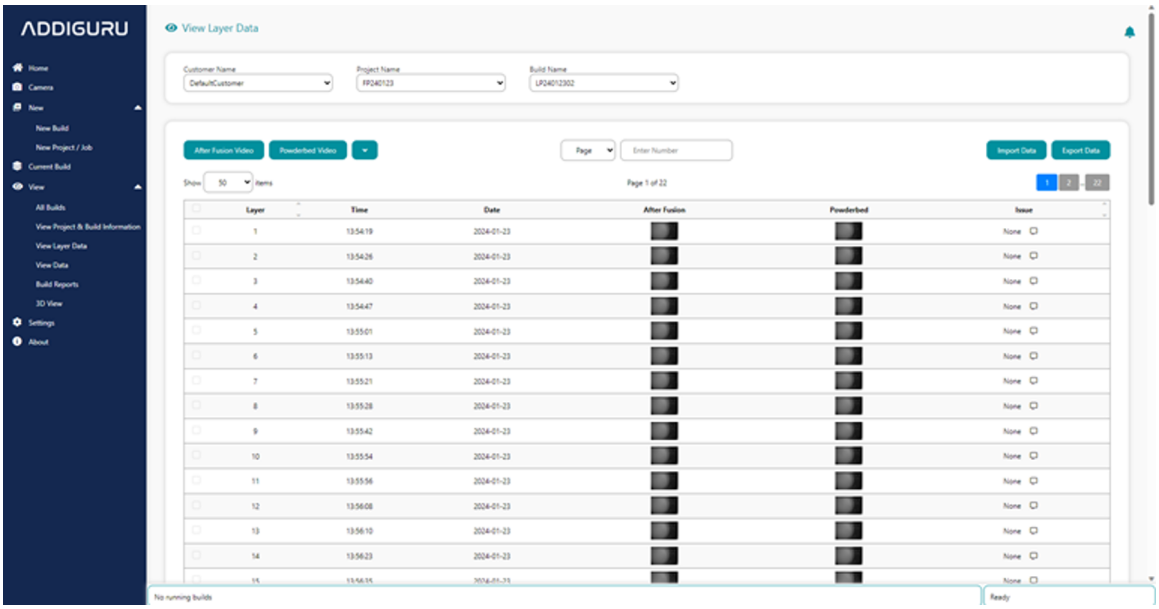
The software is designed to operate entirely independently from the L-PBF system. It does not rely on any triggers or signals from the L-PBF system, ensuring complete decoupling. The primary function of the software is to record data about the powder bed, capturing and analyzing images without any direct interaction with the L-PBF equipment. This decoupled approach allows for greater flexibility and reliability in monitoring the process, as the software's performance is not dependent on the operational status or specific triggers from the L-PBF system.

Addiguru - Optical

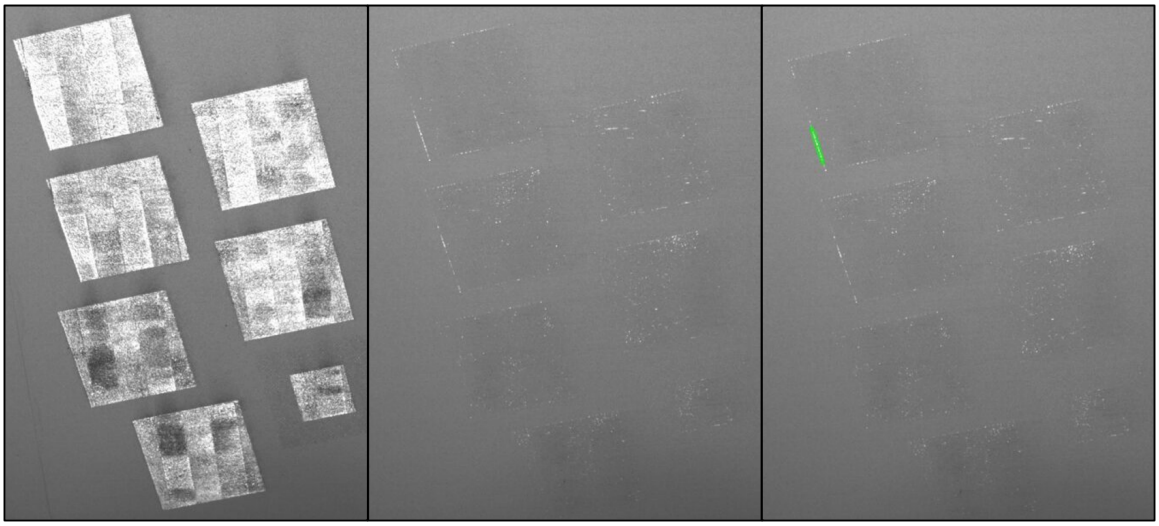
Optical data acquisition is handled by Addiguru (Addiguru, 2024). Using its proprietary technology, the software is able to take images independent of the L-PBF machine. It takes two images per layer, an image after sintering and an image after powder spreading. Utilizing proprietary machine learning models, it identifies issues such as part swelling, recoater streaking and hopping, and large spatter particles. The software shown in Figure 2.2a provides a detailed layer-by-layer view, enabling real-time monitoring and quality control. Figures 2.2b illustrate pre-spreading, post-spreading, and highlighted powder bed anomalies detected by Addiguru.

Pixelink API - NIR

To interface with the Pixelink NIR camera, the Python Pixelink API is used. The Pixelink API (Pixelink, 2024a) allows for rapid development by simplifying tasks related to camera configuration and control. The API facilitates the transfer of images to the monitoring computer in a NumPy frame, enabling the use of custom algorithms for data processing and future active build monitoring. Compared to Pixelink's



(a) Addiguru software monitoring during a build.



(b) Powder bed images with highlighted powder bed anomalies.

Figure 2.2: Addiguru optical monitoring system.

Capture software, the Python implementation offers enhanced capabilities for utilizing camera data, allowing for more sophisticated and flexible image processing and monitoring solutions in research and industrial applications. The Pixelink Capture software offers minimal analysis features, necessitating the development of custom image analysis software from scratch. Images are returned in an intensity value captured in 10 bit, corresponding to values between 0 to 1024.

Spinnaker SDK - IR

Interfacing with the FLIR A-50 is accomplished through the FLIR Spinnaker SDK Systems (2024). The Spinnaker SDK is the recommended solution for developing serious automation applications with FLIR cameras (FLIR, 2024b). Spinnaker is capable of integrating and controlling multiple FLIR cameras. The Spinnaker API supports Python which allows for more sophisticated and flexible image processing and monitoring solutions. While programs such as FLIR ResearchIR and Research Studio, discussed in the next section, offer many data analysis techniques, they can be limited in custom build functionality. Spinnaker allows for the frame to be passed as a NumPy frame so custom analysis and processing can be accomplished.

2.2 Comparison to Current Software

When recording image based data, many researchers rely on the standard programs that are generally used with the cameras. For FLIR, as seen by Table 1.1, the predominant software used is FLIR ResearchIR. While FLIR Research IR is a very capable software, it lacks customized real time monitoring. The software developed for this research wanted to emphasize the capability for future real time monitoring, hence the selection of the Spinnaker and Pixelink APIs.

Many machine OEM now offer their own platforms for in-situ such as EOS Smart Monitoring but is only available on EOS machines on a subscription based model.

This makes data collection very limited and to only layer based images as well as only data that EOS deems necessary for users to see (EOS, 2024).

2.2.1 Computer Hardware

A MSI Katana GF76 11UD-663 laptop serves as the primary computer system for data acquisition tasks. It is equipped with an Intel Core i7-11800 CPU, which features 8 cores and can reach CPU speeds of 2.4 to 4.6 GHz. The operating system installed is Windows 11. For graphical processing, the system utilizes a 4 GB NVIDIA GeForce RTX 3050 Ti Laptop GPU. Additionally, the computer was upgraded from the original 16 GB of RAM to 64 GB of DDR4 RAM operating at 3200 MHz. This specific system retailed at $1,399.99.

Chapter 3

Data Collection and Storage

3.1 Data Collection

For this project, only NIR and IR is collected in a Python script while Addiguru handles Optical data.

3.1.1 Sequential Recording

In the first iteration of the program for data acquisition, the program was written so that the NIR would capture an image at an exposure time of 200ms and then the FLIR would capture an image. This sequential process prevented the FLIR camera from achieving its full frame rate capability of 30 frames per second, as the code waited for the NIR capture to complete before retrieving a frame from the FLIR.

This led to the conclusion that a more developed script need to be created so that the NIR capture would not interfere with the FLIR and vice-versa. To accomplish this three different options were considered: multiprocessing, separate scripting, and threading.

It is more important that the NIR data is collected as complete as possible compared to the FLIR. This is due to the nature of the laser. Since it is moving at 1000 mm/sec, a dropped frame would lead to a sizable portion of the laser path

not being captured, approximately 200 mm of laser path. As the following sections will discuss, different options did not result in complete layerwise images but rather fragmented composite images.

3.1.2 Experiment outline for finalizing DAQ

To determine the feasibility of each differing recording scripts, an experiment was conducted to determine the best method for data acquisition. A standard laser pattern supplied by the Farsoon software was selected and can be observed in Figure 3.1. The laser starts the pattern on the right and then proceeds to the left. If the pattern is incomplete or degraded when a layerwise image is composed, that is a clear indicator of data loss. Three separate scripts were tested, all using different methods for computational resource allocation: multiprocessing, separate scripting, and threading.

3.1.3 Multiprocessing Recording

The first modification attempted was the multiprocessing script which utilized Python's multiprocessing library. Multiprocessing enables parallel execution of code by distributing processes across multiple cores on the same CPU, efficiently utilizing resources through balanced allocation among processor pools.

Figure 3.2, shows the composite images of the NIR images captured during the layer. In this image, the laser scans the plate from right to left. Creation of the composite images are discussed in Section 3.2.2. Figure 3.1 shows the design of the scan that was used to generate the build package. Initially, the recording system is able to captures nearly all of the images, as seen on the right of Figure 3.2 where the laser starts the layer.As the data acquisition continues to record, it fails to keep up, dropping frames, which results in fragmented composite images. These dropped frames mean that melt pool data from the build plane was not captured. This is shown in Figure 3.3 as the pull time drops to nearly zero, indicating inconsistent data

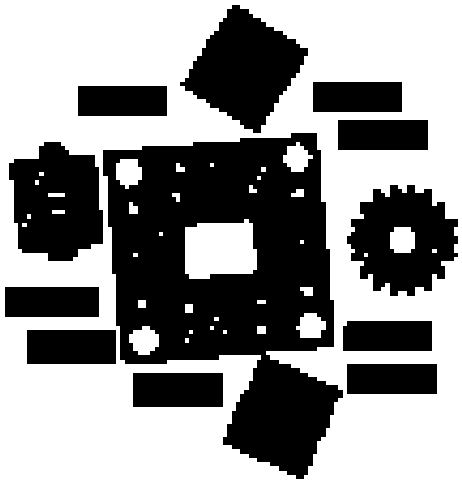


Figure 3.1: Standard laser pattern supplied by Farsoon software.

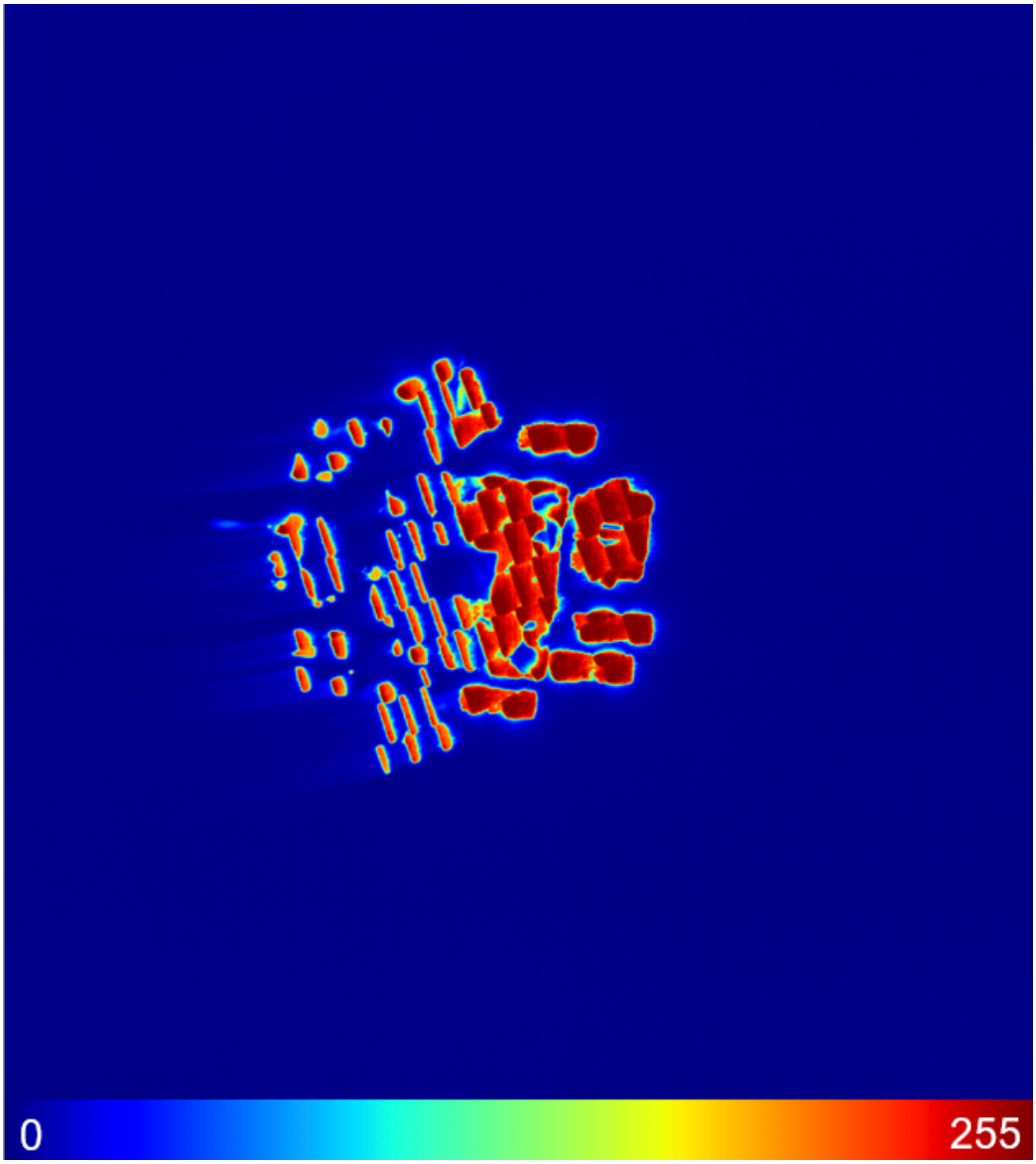


Figure 3.2: Multiprocessing layerwise image showing dropped frames.

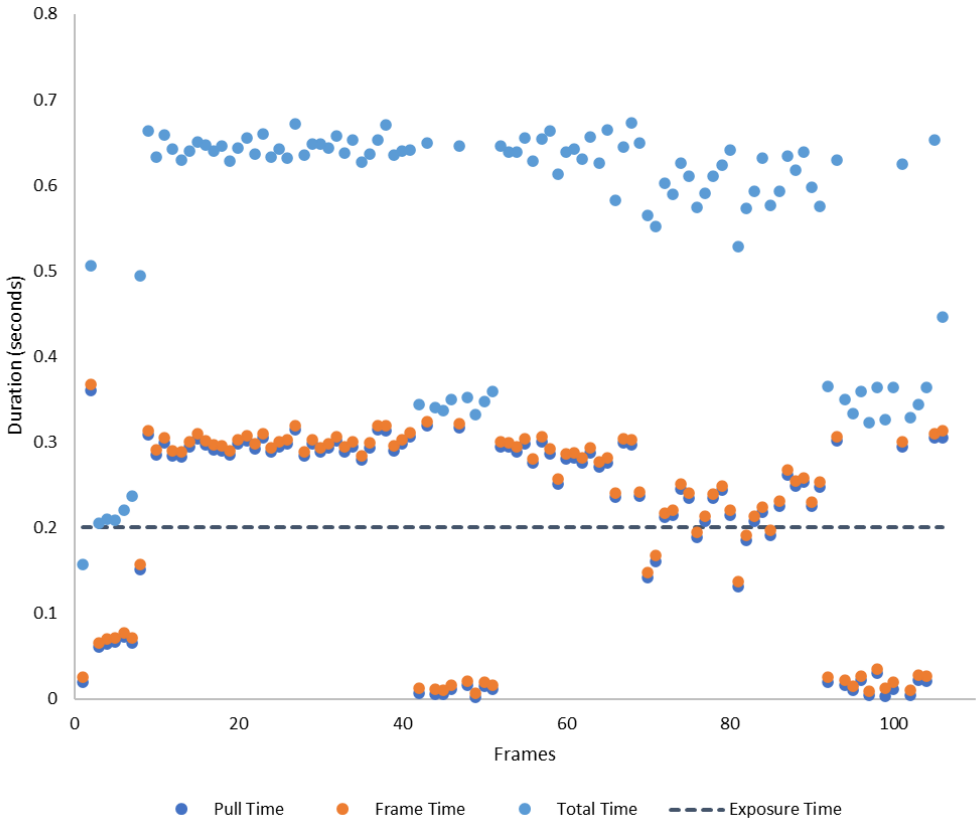


Figure 3.3: Multiprocessing timeline showing event timing during image acquisition.

acquisition and image loss. The pull time refers to the time duration necessary for image data to be transferred from the camera sensor to the DAQ computer. This image loss from multiprocessing makes sense, as multiprocessing is best suited for CPU-bound tasks that are limited by the processing power of the CPU. In contrast, I/O-bound tasks, like recording and saving images, are constrained by the speed of data input and output operations.

3.1.4 Separate Console Scripts

In this method, the data acquisition for the FLIR and NIR are decoupled from each other, each running in a separate Python console. Figure 3.4 displays this visually as a more complete image is formed, but data is still lost in the middle, indicating less dropped frames when compared to multiprocessing script. Figure 3.5 backs this up as the total time drops dramatically from frame 120 to frame 160 which corresponds to the area of fragmented images in Figure 3.4. This demonstrates that the data acquisition using separate scripts remains inadequate. This is because the Python global interpreter lock only allows one thread to be running at a time. When running two separate scripts, the computer decides which thread to allow to run at a specific instance. This leads to the computer not allocating resources in an appropriate manner needed for data acquisition.

3.1.5 Threaded Recording

The finally solution was utilizing the Python threading library. Threading takes advantage of creating multiple threads within a single process, and is best for I/O-bound tasks. A thread is single sequence of instructions that the CPU can execute. Within Python, only one thread can be executed at any time. This approach separates data acquisition between three threads, recording of the IR, recording of the NIR, and saving of the NIR images. Designating these threads allow for more control over which event is given precedent. This control allows for data acquisition to be more

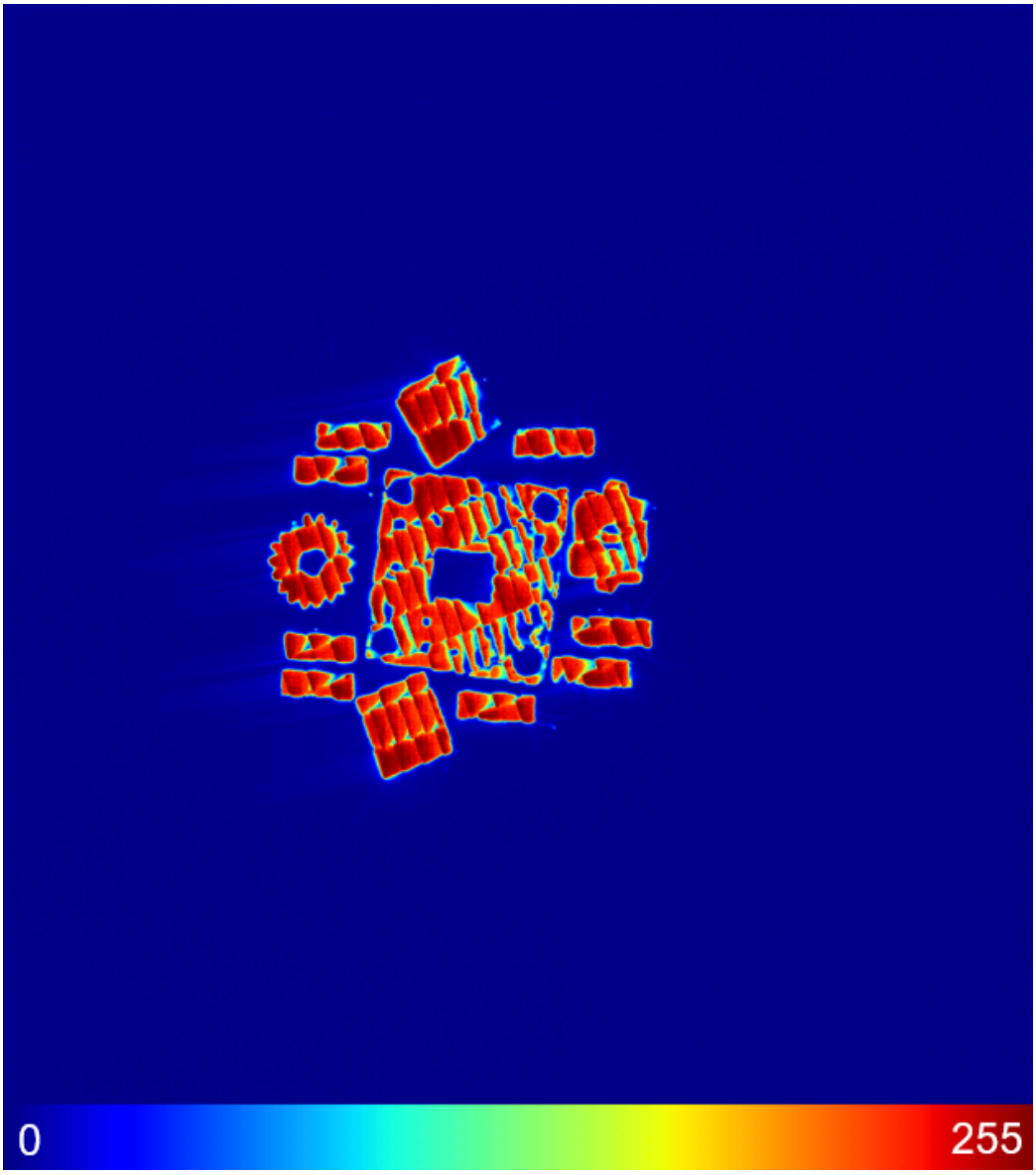


Figure 3.4: Separate script layerwise image showing reduced dropped frames.

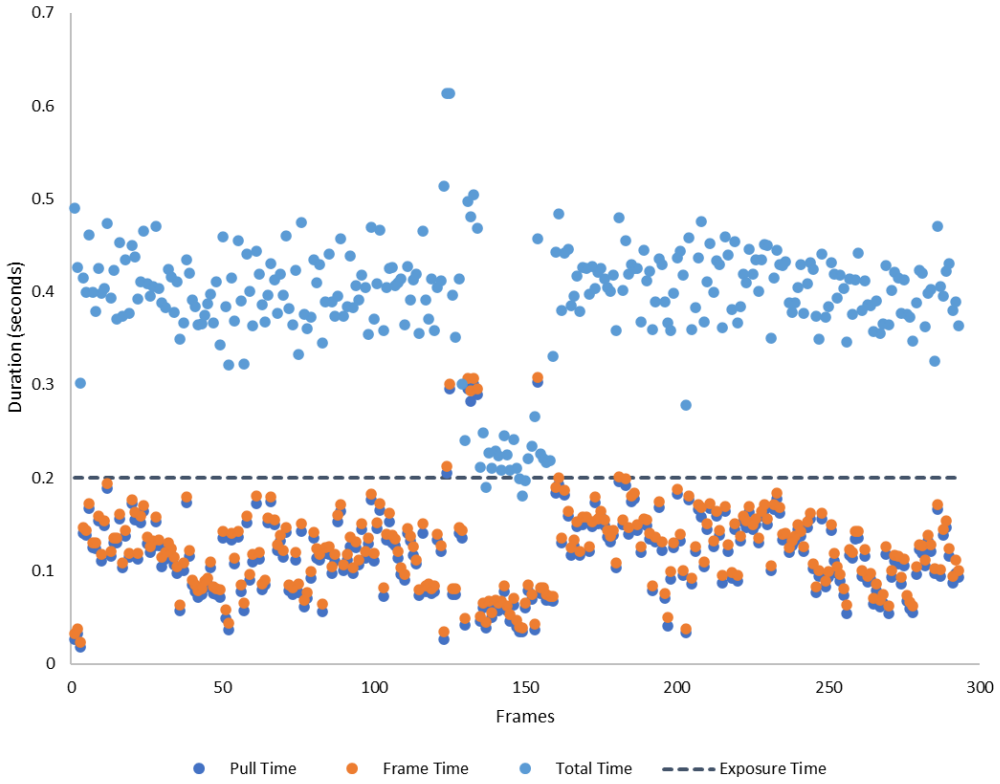


Figure 3.5: Separate script timeline showing event timing during image acquisition.

seamless, which is demonstrated by Figure 3.6, which displays the most complete image when compared to Figure 3.2 and 3.5. Figure 3.7 shows a consistent recording time with the average time between frames of the NIR being 211 ms, with 11 ms coming from the frame overhead time of the camera, which is explained in Section 3.2.2.

3.1.6 Optimized Recording Process

Based on the threaded recording script resulting in the best scripts, minor tweaks were made to refine the recording process. The finalized recording process is separated into three distinct threads: a FLIR thread, a NIR thread, and a dedicated NIR saving thread. Figure 3.8 displays the process used to record data.

The FLIR thread begins by initializing the FLIR camera and then beginning camera acquisition. This thread then saves the FLIR data and the time stamp of the FLIR image as a NumPy file. This is continued until the user terminates the program. The thread can capture and save frames at the max frame rate of 30 fps.

The NIR thread begins by initializing the Pixelink camera. After initialization, the camera begins to retrieve frames. These frames are initially in big-endian format, necessitating a byte swap to convert them to little-endian format, compatible with the Windows operating systems. After this byte swap, the images are stored in a queue. This queue is necessary as it minimizes the time between frames.

A final thread is responsible for saving the images from the queue. This queue is stored within the computer's RAM until resources are available to save the image. This allows for the program to be adaptable and if a process starts taking up resources, the RAM can be used for images to be held until saving can be accomplished, which is a resource-intensive process. This process can be resource-intensive due to the high amount of I/O operations being conducted while DAQ is occuring.

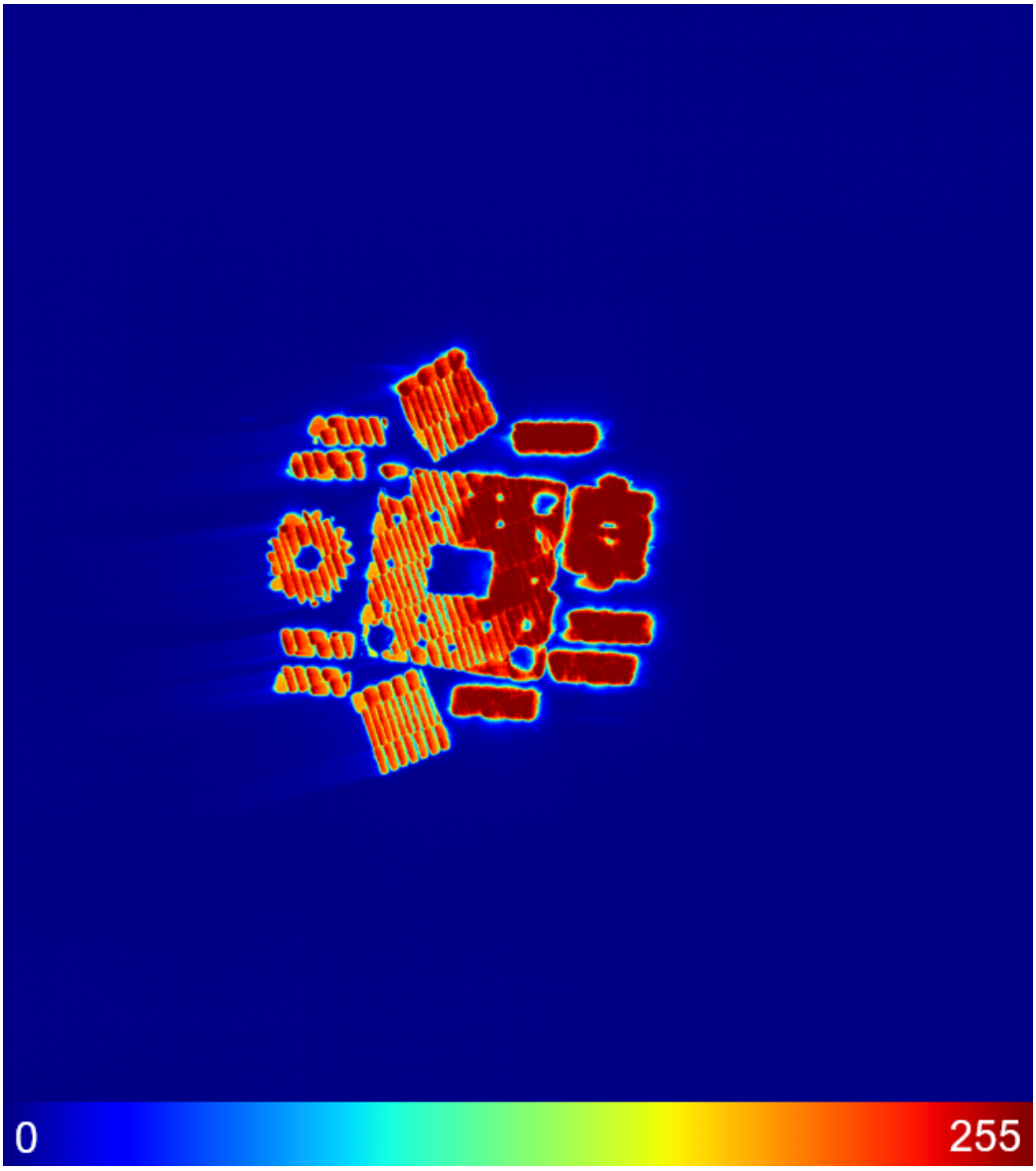


Figure 3.6: Threading script layerwise image.

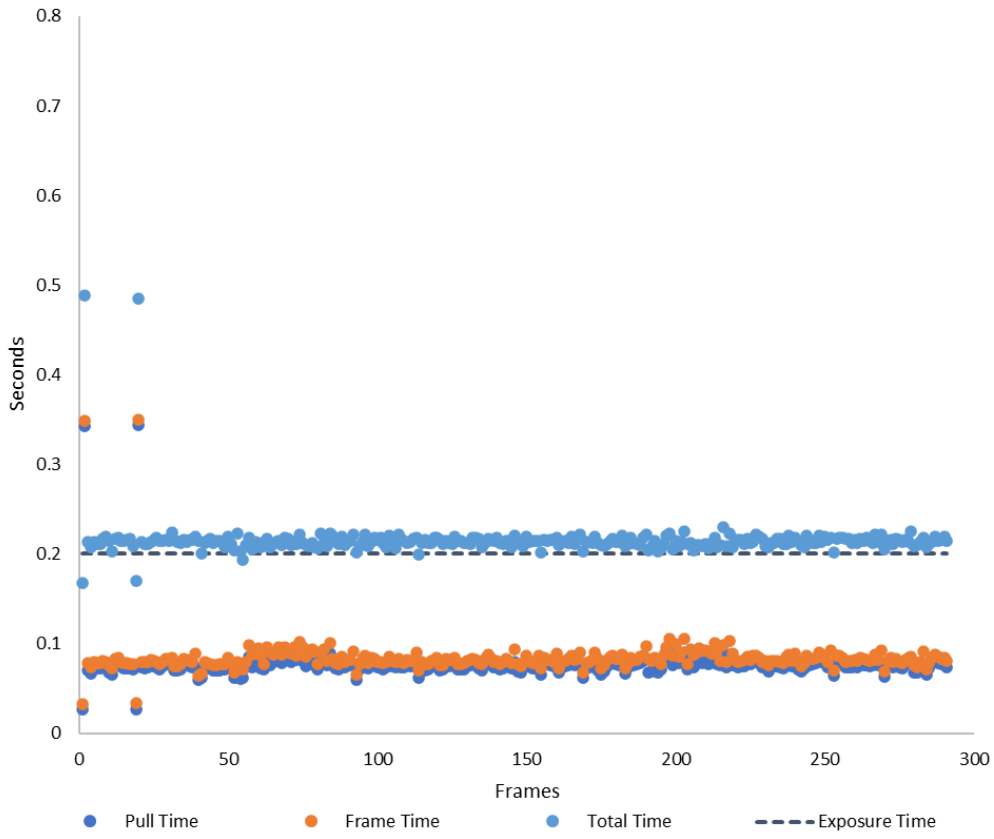


Figure 3.7: Threading script event timeline during image acquisition.

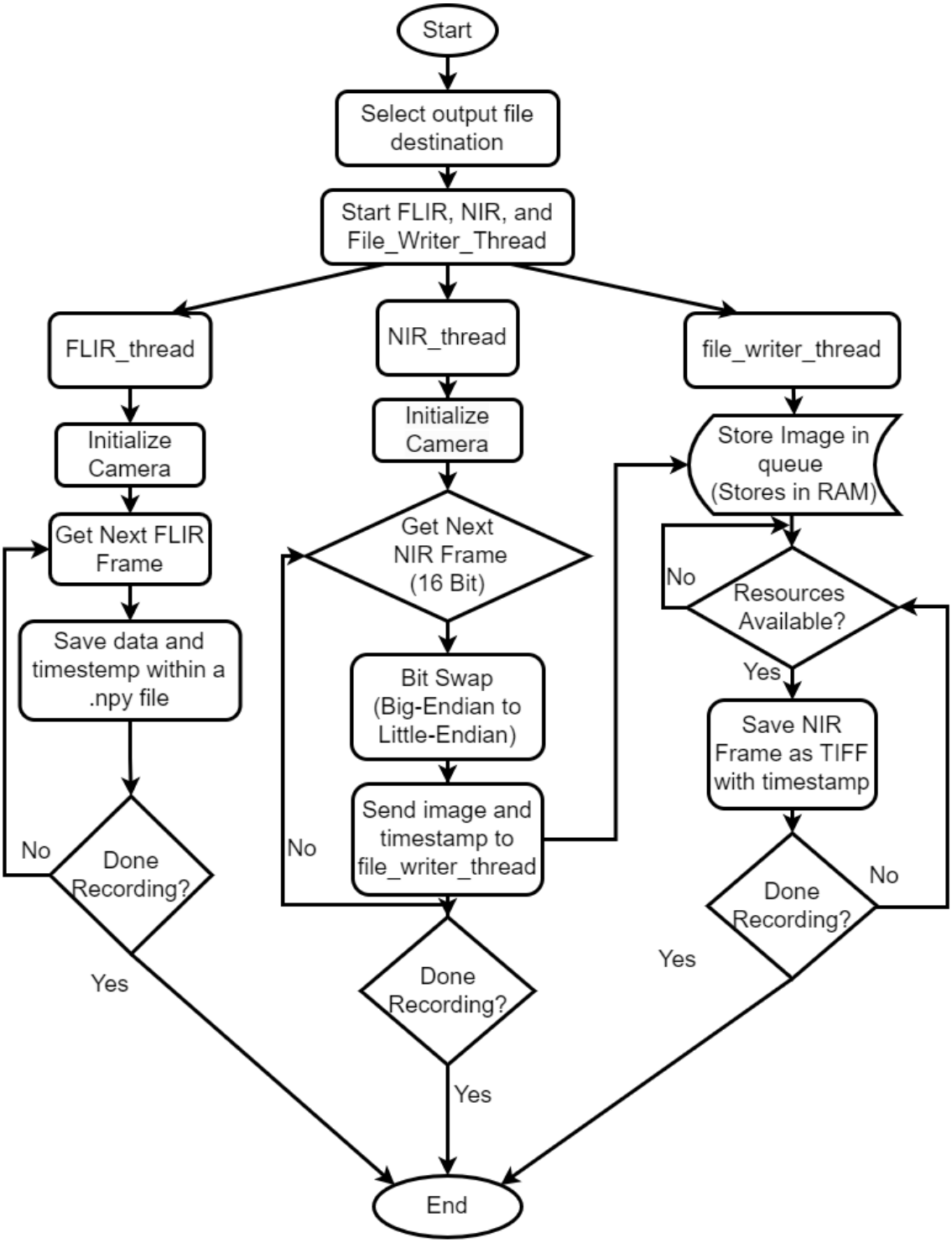


Figure 3.8: Data acquisition process flow.

3.2 Data Collected

3.2.1 Optical

Data collection for the optical modality only consists of two images per layer: one image before powder spreading, and one image post powder spreading. These images are processed using Addiguru's proprietary machine learning computer vision algorithm to detect potential powder bed defects. These images also can be exported as raw optical images as well.

3.2.2 NIR

NIR data collection consists of images taken at an exposure time of 200 ms. Due to certain optical filters being on the NIR camera, the intensity of the images increase only when the laser is actively sintering. Utilizing this information, along with buffers and gap detection (to account for instances when the laser is not captured in a frame but the layer is not complete), a layer-wise image is generated.

NIR Image Layer Creation

To determine where layers occur in the NIR data, the maximum pixel intensity is examined to determine when the laser is on. This occurs where there is an increase in the maximum pixel intensity between frames. Layers are detected based on this increase, and in turn, decrease when the laser is done firing. After the layers are detected based on the intensity levels of the images. This script uses the 'numpy.max' function to compare two NumPy arrays, identifying the maximum intensity values at each pixel location between the two frames. By doing so, it generates a composite image that combines the most prominent features from both input images. The algorithm for comparing two matrices and determining the maximum values is detailed in Equations 3.1 and 3.2. This algorithm is visually shown in Figure 3.9. The result is a detailed representation that highlights the highest intensity levels,

allowing for a more comprehensive analysis and visualization of the combined data. This process is then repeated for every frame in the layer, creating a image of the maximum values in a layer. These layerwise images allow for more efficient data storage and allows for easier correlation to process events due to the layerwise nature of the image. Since the only increase in intensity is from either spatter or the laser sintering due to the optical lenses on the camera, spatter and meltpool intensity events are captured.

$$\text{Let } A = [a_{ij}] \text{ and } B = [b_{ij}] \text{ be two matrices of the same dimensions.} \tag{3.1}$$

$$\text{Let } C = \max(A, B) \text{ where } C = [c_{ij}] \text{ and } c_{ij} = \max(a_{ij}, b_{ij}). \tag{3.2}$$

Frame Overhead Time

Due to the restrictions of the physical camera, there are inevitable time durations during which the camera cannot record, commonly referred to as Frame Overhead Time (FOT). As a result, melt pool information is not captured during the FOT, producing data "gaps," as illustrated in Figure 3.10. FOT gaps occur because of the camera's global shutter mechanism and its sequential reading of its sensor data. Once sensor data is captured during the prescribed exposure time, the image must be read out of the camera sensor, during which time the camera sensor cannot record additional light collection at the sensor. This process is done sequentially and is a function of several factors, including the Region of Interest (ROI), the number of Low Voltage Differential Signaling (LVDS) taps, decimation, and the clock period of the camera. Among these factors, the ROI is the only variable that can be adjusted by the user, while the number of LVDS taps, decimation, and clock period of the camera remain constant and dependent fully on the camera. Reducing the ROI directly reduces the FOT, thereby minimizing the data gaps. For this the full ROI, this FOT is 11ms.

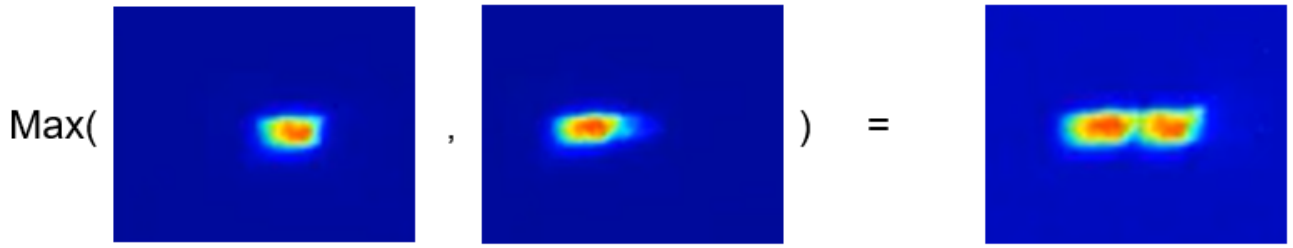


Figure 3.9: Visual representation of 'numpy.max' algorithm.

The equations governing FOT provide a mathematical framework for understanding these gaps. Specifically, FOT is calculated using the equation:

$$\text{FOT} = \text{Row Time} \cdot (\frac{\text{Height}}{\text{Decimation}}) \tag{3.3}$$

where Row Time is defined as:

$$\text{Row Time} = \frac{\text{Max Width}}{\text{Decimation}} \cdot \frac{\text{Clock Period}}{\text{\# of LVDS taps}} + 2 \cdot \text{Clock Period} \tag{3.4}$$

and Height is the height of the image, Max Width is the maximum width of the captured image, decimation is the reduction in the number of pixels in an image, and the clock period is defined as the discrete number of cycles per second in which the camera can update. internal clock These equations illustrate that the FOT depends on the row time, which itself is influenced by the width of the image, the decimation factor, the clock period, and the number of LVDS taps. LVDS taps in a camera refer to multiple parallel data channels that transmit high-speed image data from the camera sensor to the processor. This shows that the only factors that could be changed to reduce is the height and width, which are the parameters of the ROI (Pixelink Support, 2024). Figure 3.11 shows the FOT for 5% increments of the max width and height to 50% of the max width and height.

3.2.3 FLIR

Data is collected from the FLIR A50 camera in raw intensity counts. To get a Celsius temperature value from these intensity values, Equation 3.5 is used. Within this equation, K_1 represents the inverse of the product of the atmospheric transmittance, emissivity of the object, and the transmission of the external optics. K_2 represents the sum of the pseudo radiance of the reflected environment, pseudo radiance of the atmosphere, and the pseudo radiance of the external optics. These values are dependent on the emissivity of the object, the temperature of the atmosphere, the

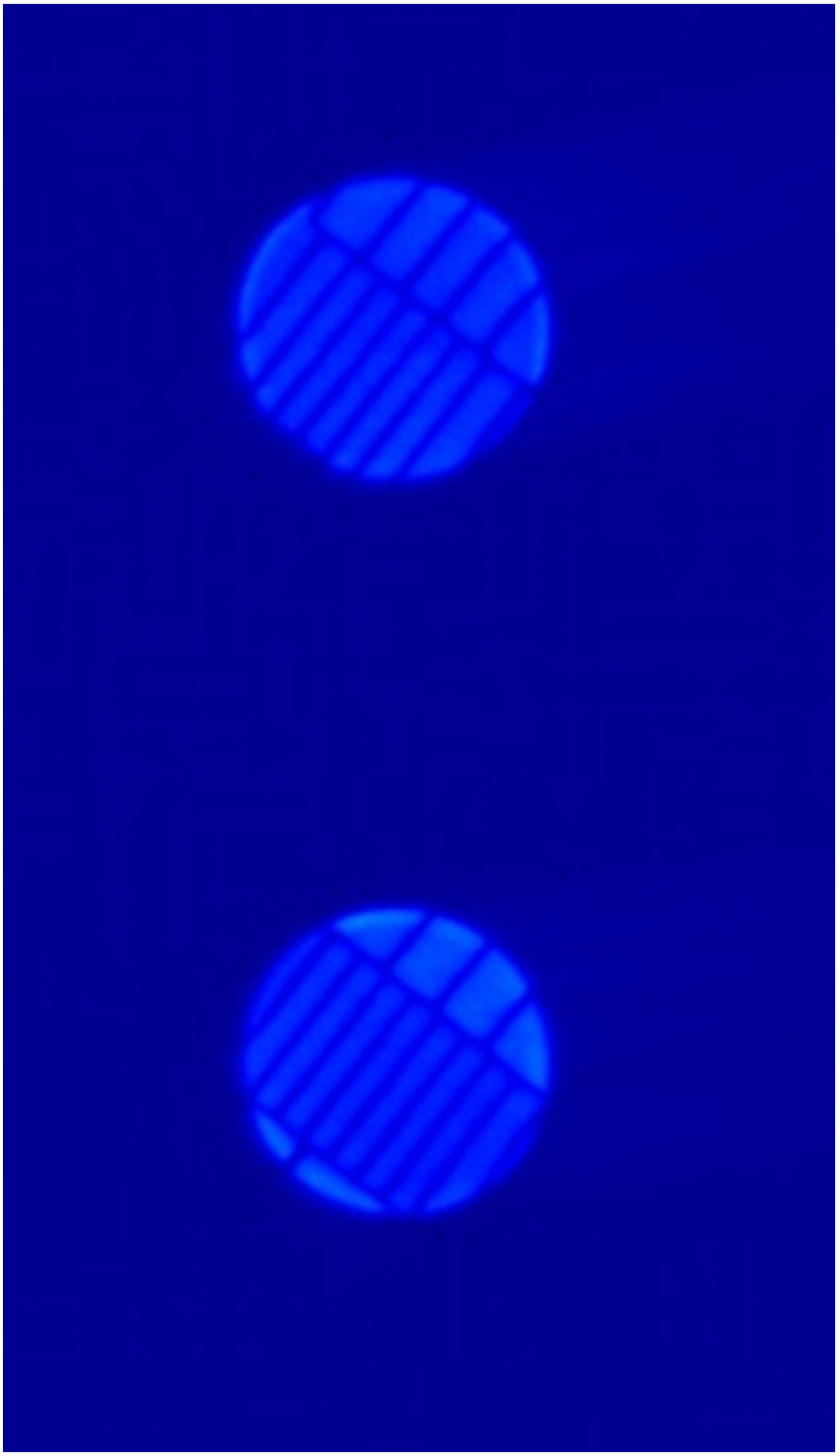


Figure 3.10: Example of data gaps due to FOT. A layerwise NIR image of a circular part from layer 234 reveals line gaps that interrupt the full circular silhouette. These gaps indicate areas where data could not be collected during the frame overhead time.

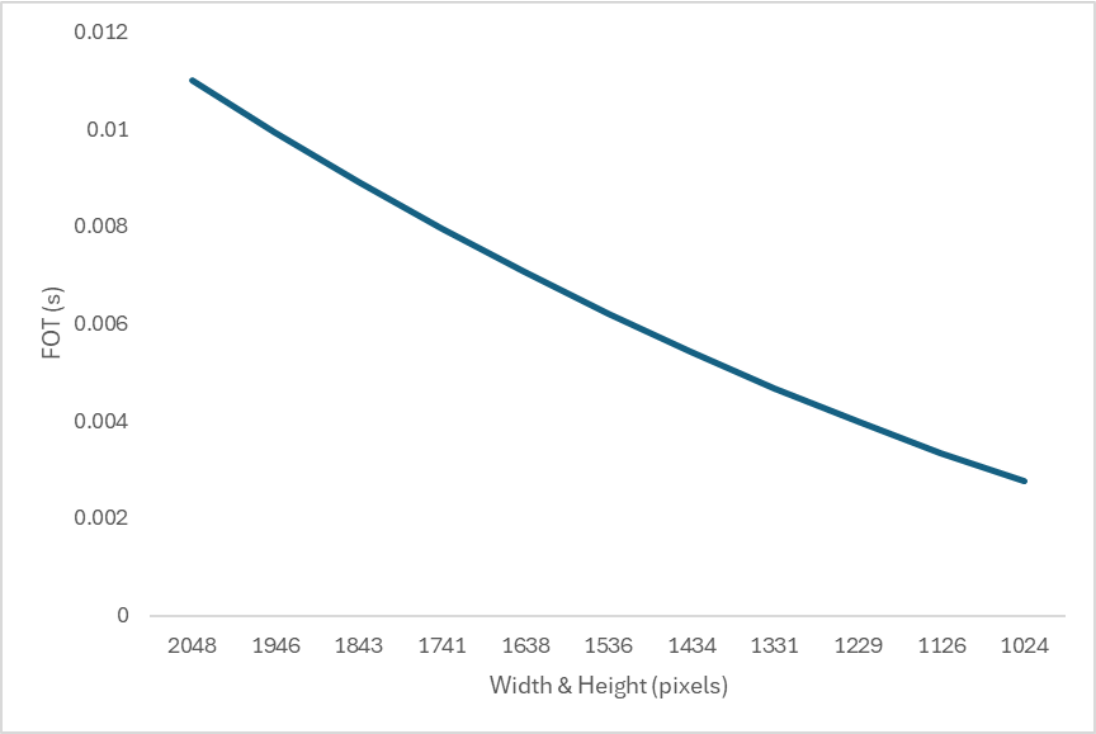


Figure 3.11: FOT in 5% increments of the max width and height to 50% of the max width and height.

humidity, and efficient temperature of a complex surrounding. Further explanation of these values can be found in (FLIR-Systems, 2024). R, B, F, J_1, and J_0 depend on the FLIR camera and temperature range cases and are retrieved from the calibration variable that are stored within the camera memory (FLIR-Systems, 2024).

$$T_{\text{Celsius}} = \frac{B}{\log(\frac{R}{K_1 \cdot (\frac{\text{Intensity} - J_0}{J_1}) - K_2} + F} - 273.15 \tag{3.5}$$

FLIR frames are recorded and saved in a NumPy frame with the time stamp when the image is recorded.

3.3 Data Storage

3.3.1 HDF5 Format

After all process monitoring images are collected as NumPy arrays and the data acquisition is stopped, the Hierarchical Data Format version 5, HDF5, is used to format the data for storage compactly. HDF5 is a versatile data storage file format designed to store and manage large and complex datasets in an efficient manner. Its hierarchical structure enables the organization of data into groups and datasets, similar to how a file system is organized, which allows for simplification of the management of intricate data collections.

HDF5 is highly efficient, offering fast access and built-in loss-less compression to reduce storage needs without compromising data integrity. Additionally, it is cross-platform, facilitating data sharing and collaboration. The inclusion of rich metadata enhances context and data analysis, while support for parallel I/O operations makes it suitable for high-performance computing applications (The HDF Group, 2024).

Due to the potentially large dataset generated for this project, where some file archives can be over 500GB for a single build, the FLIR and NIR data is split into two separate HDF5 file. This allows for the independent downloading and storage of

each modality. This approach not only facilitates efficient data management but also enables storage on separate drives, accommodating the substantial size of the files.

3.3.2 Compression

Since datasets can be quite large as data is collected in a raw, data-rich format, HDF5 loss-less compression is necessary. The compression algorithm used to accomplish this is gzip. Gzip is a widely-used compression algorithm that reduces the size of data by identifying and eliminating redundant information. It operates using a combination of the LZ77 algorithm and Huffman coding, achieving efficient and fast compression. Gzip is particularly valuable in research and data management for minimizing storage requirements and enhancing data transfer speeds (Gzip-Project, 2024).

3.3.3 Optical Data Storage

Optical data from Addiguru are currently compressed to a .zip folder. These optical images are raw frames with no post processing or identification done via the Addiguru algorithm. These are then stored in the same file location as the HDF5 archive. Future work will be to convert these images to an HDF5 archive.

3.3.4 Long Term Storage

Our research group's long term storage and data management system consists of one processing computer, one server, and Microsoft Teams Cloud Storage. Data is compressed utilizing the processing computer. If processing of the data needs to be immediate, the HDF5 archive can be copied locally to the processing computer. If short-term processing is unnecessary or local storage is insufficient, the HDF5 is uploaded to the server. The server is connected to the processing computer via a 10 GB fiber connection, allowing for high speed transfer rates. If processing is complete on the data, then data can be uploaded for long term storage to Microsoft Teams Cloud Storage.

Chapter 4

Calibration Plate and Perspective Correction

4.1 Objective

The primary objective of this study is to introduce a low-cost, multi-modal calibration plate designed to enhance in-situ monitoring of L-PBF processes. This calibration plate aims to provide an efficient and cost-effective solution for overlaying data from three different modalities: optical, NIR, and IR cameras, enabling easy comparison and data fusion. The expected benefits include improved accuracy and reliability of in-situ monitoring, ultimately contributing to better quality assurance in L-PBF manufacturing.

4.2 Calibration Plate

The calibration plate, seen in Figure 4.1 is designed with a series of circular holes that can be easily detected by OpenCV, an open-source computer vision Python library. The circles measure 8mm in diameter and are spaced 20 mm from center to center in both the x and y directions. The plate measures 24.13 x 29.21 cm and has a

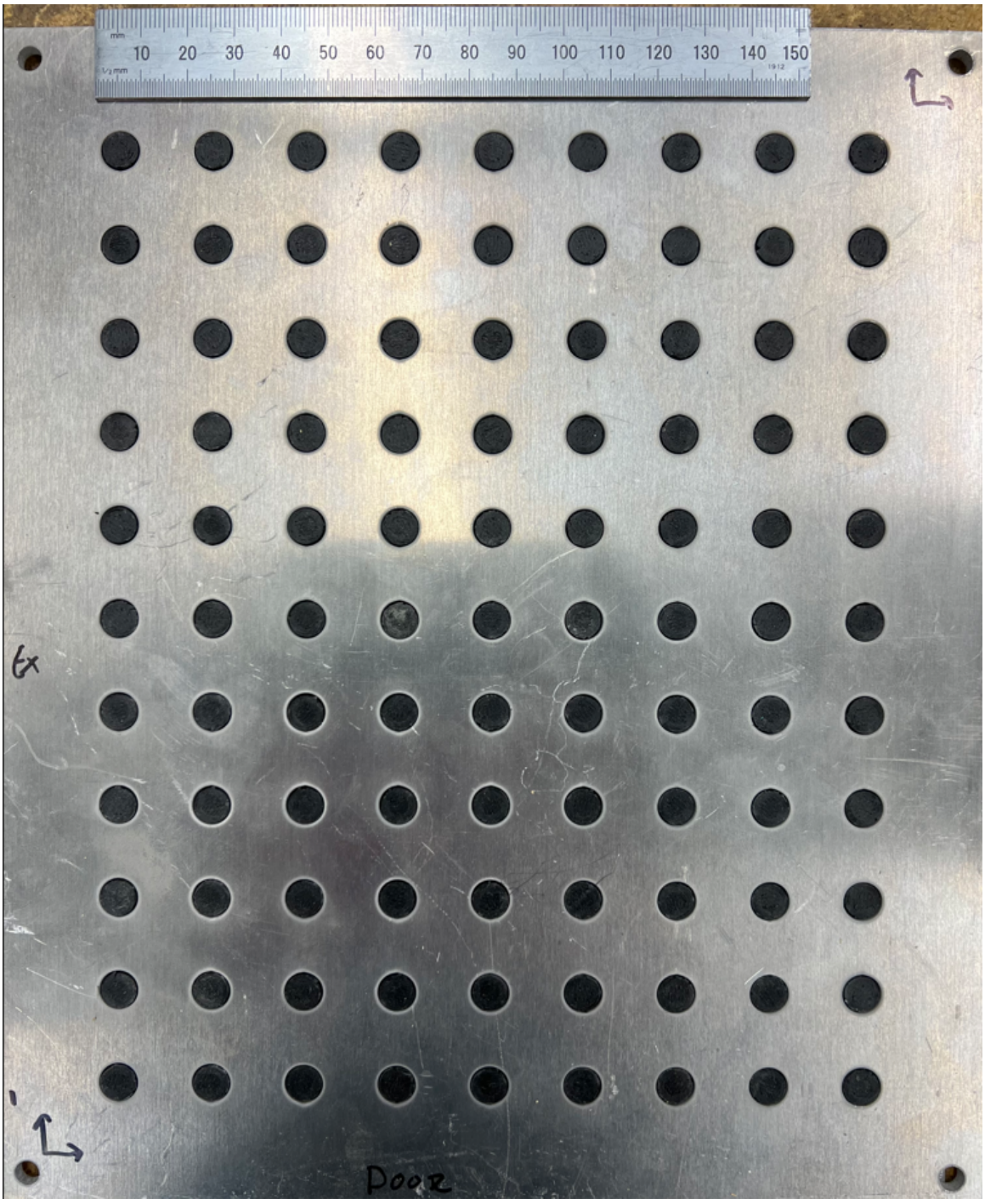


Figure 4.1: Manufactured Calibration Plate with 155 mm ruler for scale.

thickness of 0.3175 cm. The circle pattern design was generated using OpenCV's calibration pattern generator. The plate circles are then located using OpenCV's built-in circular grid detector, which detects the shape of each circle and calculates its center, allowing for precise linear transformations of the image plane based on the grid of circles. The materials chosen for the calibration plate include polyvinyl chloride (PVC) and stainless steel, selected for their different emissivity values. The difference in emissivity between these materials allows for clear imaging by optical and infrared cameras, facilitating accurate calibration across different spectral ranges. The manufacturing process of the calibration plate involved machining via a water jet to create circular patterns within the stainless-steel plate. After this step is completed, printed PVC plugs were inserted into these holes to allow for the differing emissivity. The accuracy of the water jet is 0.127mm. The calibration plate is made with a 9 by 11 grid of circles in a symmetric pattern.

4.3 Data Collection

4.3.1 Hardware Used

The calibration plate is used to perspective correct the three cameras used in this research: the Basler acA5472-17um, Pixelink PL-D734MU-NIR-T, and the FLIR A50. Further information about the camera can be found in Section 2.1.2. These cameras are positioned within a Farsoon 271M L-PBF machine to capture different modalities of L-PBF processing. Integration considerations include proper mounting, cable routing, and the placement of the calibration plate to ensure optimal data capture.

The calibration plate is designed to accommodate multiple camera angles, enabling different camera mounting configurations used within not only the Farsoon 271M but various other L-PBF systems. This flexibility ensures that the calibration process

can be adapted to different setups, enhancing the applicability and usability of the calibration plate across different machines and mounting points.

4.3.2 Pinhole Camera Model

In this study, the camera is approximated using the OpenCV pinhole camera model, visually shown in Figure 4.2. This model accounts for a distortion-free projection transformation (Bradski, 2000).

A distortion-free projection transformation given by a pinhole camera model can be described as:

$$s\,\mathbf{p} = \mathbf{A}\,[\mathbf{R} \mid \mathbf{t}]\,\mathbf{P}_w \tag{4.1}$$

Where $\mathbf{P}_w$ is a 3D point expressed in relation to the world coordinate system, $\mathbf{p}$ is a 2D pixel from the corrected image plane, $\mathbf{A}$ is the camera intrinsic matrix, $\mathbf{R}$ is the rotation matrix of the image, $\mathbf{t}$ is the translation matrix of the image, and s is the projection scaling factor of the image. The camera intrinsic matrix $\mathbf{A}$ projects the 3d points given in the camera coordinate system, $\mathbf{P}_c$, to 2D pixel coordinates, $\mathbf{p}$:

$$\mathbf{p} = \mathbf{A}\mathbf{P}_c \tag{4.2}$$

For a pin-hole model camera, A is composed of the camera focal lengths f_x and f_y expressed in pixel units and the principal point (c_x, c_y) which is typically close to the image center:

$$\mathbf{A} = \begin{bmatrix} f_x & 0 & c_x \\ 0 & f_y & c_y \\ 0 & 0 & 1 \end{bmatrix} \tag{4.3}$$

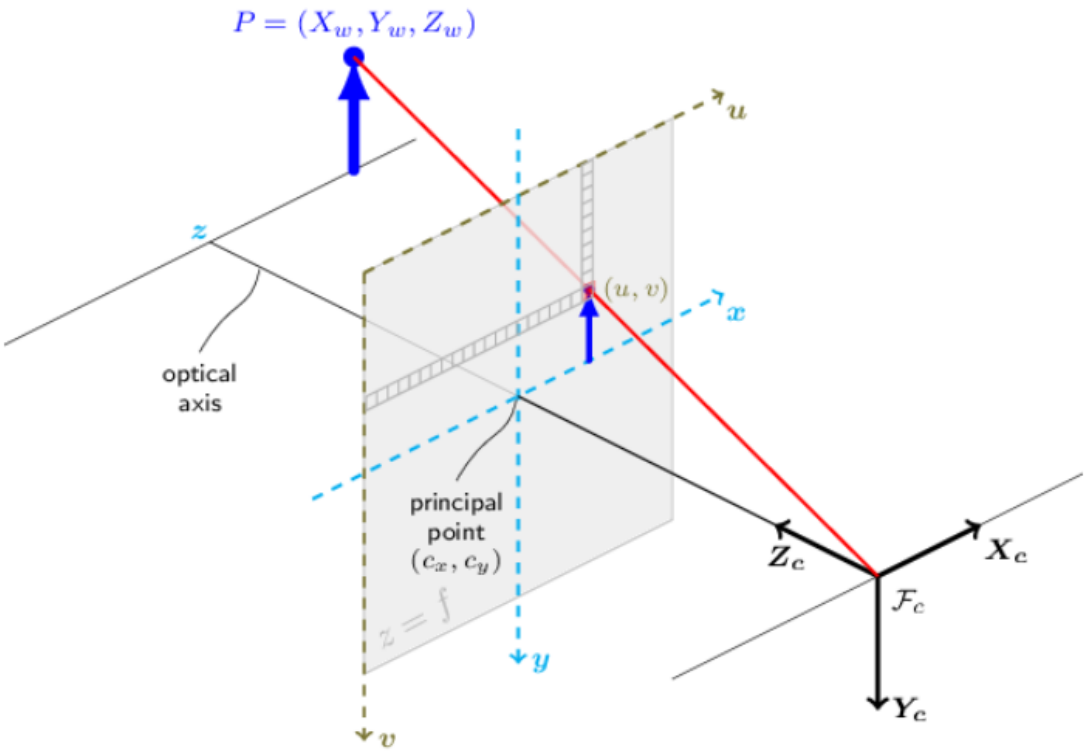


Figure 4.2: Pinhole camera model (Bradski, 2000).

Combining the above equations yields, where u and v are 2D image coordinates:

$$s \begin{bmatrix} u \\ v \\ 1 \end{bmatrix} = \begin{bmatrix} f_x & 0 & c_x \\ 0 & f_y & c_y \\ 0 & 0 & 1 \end{bmatrix} \begin{bmatrix} X_c \\ Y_c \\ Z_c \end{bmatrix} \tag{4.4}$$

The rotation-translation matrix $[\mathbf{R} \mid \mathbf{t}]$ is the matrix product of a projection transformation and a homogeneous transformation. This maps the 3D points represented in camera coordinates to 2D points in the image plane and are represented in normalized camera coordinates $x' = X_c/Z_c \quad \text{and} \quad y' = Y_c/Z_c$:

$$Z_c \begin{bmatrix} x' \\ y' \\ 1 \end{bmatrix} = \begin{bmatrix} 1 & 0 & 0 & 0 \\ 0 & 1 & 0 & 0 \\ 0 & 0 & 1 & 0 \end{bmatrix} \begin{bmatrix} X_c \\ Y_c \\ Z_c \\ 1 \end{bmatrix} \tag{4.5}$$

The homogeneous transformation is defined by the extrinsic parameters $\mathbf{R}$ and $\mathbf{t}$ and facilitates the conversion of coordinates from the world coordinate system to the camera coordinate system. Given a point P in world coordinates, denoted as $\mathbf{P}_w$, its corresponding representation in the camera coordinate system, $\mathbf{P}_c$ can be calculated using:

$$\mathbf{P}_c = \begin{bmatrix} \mathbf{R} & \mathbf{t} \\ \mathbf{0} & 1 \end{bmatrix} \mathbf{P}_w. \tag{4.6}$$

The homogeneous transformation is composed out of $\mathbf{R}$ and $\mathbf{t}$ which can be described by the matrix:

$$\begin{bmatrix} \mathbf{R} & \mathbf{t} \\ \mathbf{0} & 1 \end{bmatrix} = \begin{bmatrix} r_{11} & r_{12} & r_{13} & t_x \\ r_{21} & r_{22} & r_{23} & t_y \\ r_{31} & r_{32} & r_{33} & t_z \\ 0 & 0 & 0 & 1 \end{bmatrix}. \tag{4.7}$$

Combining Equations 4.6 and 4.7 yields:

$$\begin{bmatrix} X_c \\ Y_c \\ Z_c \\ 1 \end{bmatrix} = \begin{bmatrix} r_{11} & r_{12} & r_{13} & t_x \\ r_{21} & r_{22} & r_{23} & t_y \\ r_{31} & r_{32} & r_{33} & t_z \\ 0 & 0 & 0 & 1 \end{bmatrix} \begin{bmatrix} X_w \\ Y_w \\ Z_w \\ 1p \end{bmatrix}. \tag{4.8}$$

Combining the projection transformation and the homogeneous transformation, the projection transformation that maps 3D points in world coordinates into 2D points in the image plane is obtained and in normalized camera coordinates:

$$Z_c \begin{bmatrix} x' \\ y' \\ 1 \end{bmatrix} = \begin{bmatrix} \mathbf{R} \mid \mathbf{t} \end{bmatrix} \begin{bmatrix} X_w \\ Y_w \\ Z_w \\ 1 \end{bmatrix} = \begin{bmatrix} r_{11} & r_{12} & r_{13} & t_x \\ r_{21} & r_{22} & r_{23} & t_y \\ r_{31} & r_{32} & r_{33} & t_z \\ 0 & 0 & 0 & 1 \end{bmatrix} \begin{bmatrix} X_w \\ Y_w \\ Z_w \\ 1 \end{bmatrix} \tag{4.9}$$

with $x' = \frac{X_c}{Z_c}$ and $y' = \frac{Y_c}{Z_c}$. Putting the equations for intrinsic and extrinsic parameters together, $s\mathbf{p} = \mathbf{A}\left[\mathbf{R} \mid \mathbf{t}\right]\mathbf{P}_w$ can be written as

$$s \begin{bmatrix} u \\ v \\ 1 \end{bmatrix} = \begin{bmatrix} f_x & 0 & c_x \\ 0 & f_y & c_y \\ 0 & 0 & 1 \end{bmatrix} \begin{bmatrix} r_{11} & r_{12} & r_{13} & t_x \\ r_{21} & r_{22} & r_{23} & t_y \\ r_{31} & r_{32} & r_{33} & t_z \\ 0 & 0 & 0 & 1 \end{bmatrix} \begin{bmatrix} X_w \\ Y_w \\ Z_w \\ 1 \end{bmatrix} \tag{4.10}$$

The term $\mathbf{A}\left[\mathbf{R} \mid \mathbf{t}\right]$ is also known as the homography matrix which can be represented as $\mathbf{H}$. The tomography matrix can be found in OpenCV using the "findHomography" function. An example of an $\mathbf{H}$ value generated by OpenCV can be seen below:

$$\mathbf{H} = \begin{bmatrix} 8.34479207 \times 10^{-1} & 6.22027312 \times 10^{-2} & 8.64884678 \times 10^{1} \\ -2.22416516 \times 10^{-1} & 9.11115946 \times 10^{-1} & 4.37825116 \times 10^{2} \\ -1.17010869 \times 10^{-4} & -5.32667372 \times 10^{-6} & 1 \end{bmatrix} \tag{4.11}$$

4.3.3 Calibration Process

To begin the calibration process, the calibration plate is mounted into place and an image is collected from the camera of interest. Once the image of the calibration plate is taken, and the OpenCV function "findCirclesGrid" is applied to obtain the location of each circles center of the calibration plate captured by the camera. A second list of points, representing the ground truth, is needed for the next function. This ground truth is generated by a simple script that uses the expected center points of a grid of circles, assuming the plan of the grid of circles is on-axis.

These two lists of points are then fed into the OpenCV "findHomography" function to calculate the homography matrix. Once calculated, this homography matrix can be used to correct any image, as long as the camera remains stationary. The OpenCV function"warpPerspective" is then used to unwarp the image, utilizing the homography matrix to correct the image as if viewed on-axis. During this process, the dimensions of the destination plane image are used to resize the image. It is important to consider this resizing, as it may downscale or upscale the image. To achieve an image most similar to the original, the destination image dimensions should be similar in pixel size to the original image. This allows for transforming all images to a common size, facilitating easy comparison between modalities, with a near 1-to-1 pixel correspondence. Figure 4.3 shows a flowchart of the algorithm.

IR Specific Details

The field of view of the FLIR A50 camera is limited due to the constrained size of the build chamber and limits on the camera distance to the build plate. Thus, only a portion of the calibration plate, i.e. eight rows instead of nine, is visible in a single image. This issue is resolved by removing the corresponding circles in the target image. The NIR and optical cameras have a field of view that encompasses the entirety of the calibration and build plate.

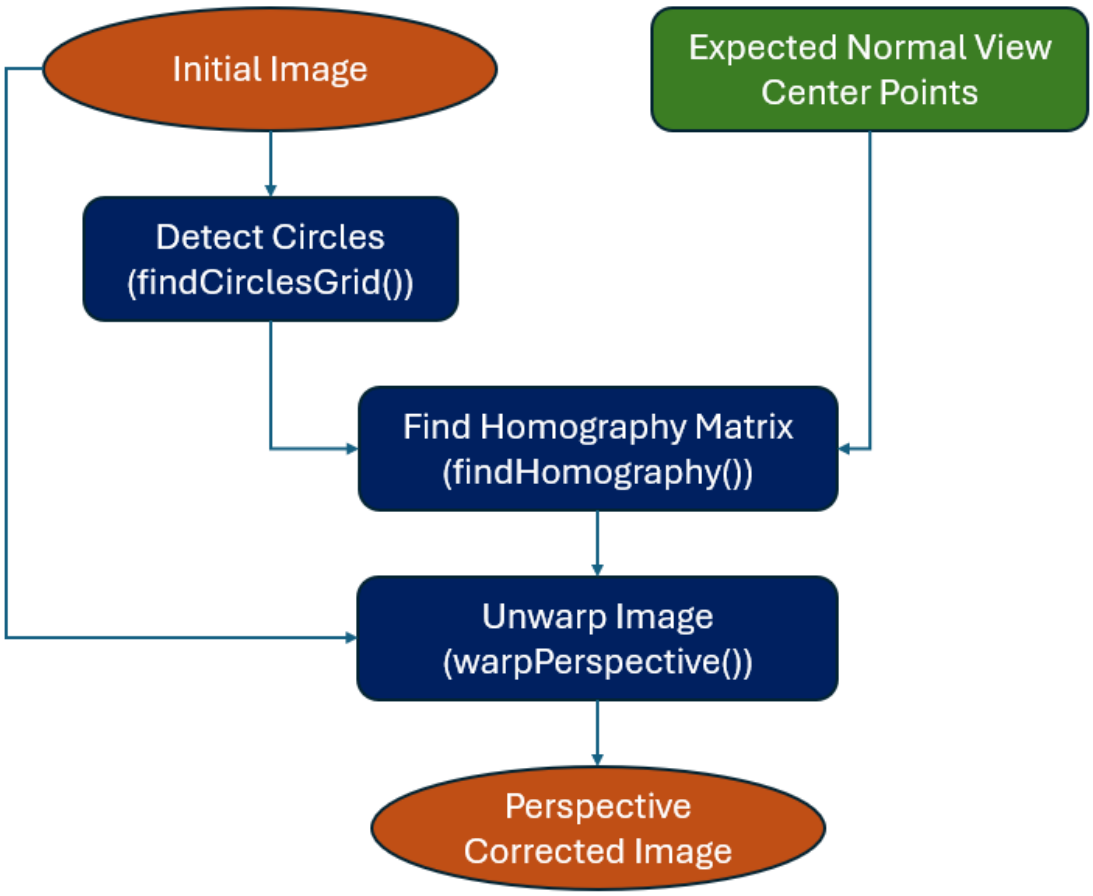


Figure 4.3: Flowchart for perspective transform of images.

4.4 Results and Discussion

4.4.1 Initial Findings

The main purpose behind this analysis is to be able to overlay images and quantify any residual lens distortion present in the perspective corrected image. This will allow a near 1-to-1-pixel correspondence between camera images, allowing direct correspondence of defects across image modalities. To accomplish this, all images are downscaled. The optical and NIR are downscaled to a common resolution of 1000 x 1200 pixels. The FLIR is downscaled to a resolution of 300 by 350 pixels.

NIR Results

The initial NIR image, seen in Figure 4.4 was transformed to a resolution of 1000 by 1200 pixels from an original resolution of 2048 by 2048 pixels. In Figure 4.5, the initial NIR image (red in the image) was then overlayed with the mathematical-based model of the plate (green). To determine the accuracy of the transform, the center of the perspective-transformed circles were then found and compared to the nominal centers of the circle by taking the difference between the center locations. Figure 4.6 displays the displacement of the differences between centers in pixels, magnified by a scalar value of 10 for ease of viewing. Figure 4.6 shows that the error plots follow a pattern expected for aberrations in camera optics. Since this calibration only addresses distortion free images, it is incapable of fully correcting these common optical errors (Choi et al., 2006). The maximum error displacement was 1.105 mm with the average error being 0.312 mm. Figure 4.7 displays the distribution in the measured error, showing that the vast majority of the error is under 0.500 mm. The reprojection error of the optical transform is represented by a scatter plot that displays the x and y error components in pixels can be seen in Figure 4.8.

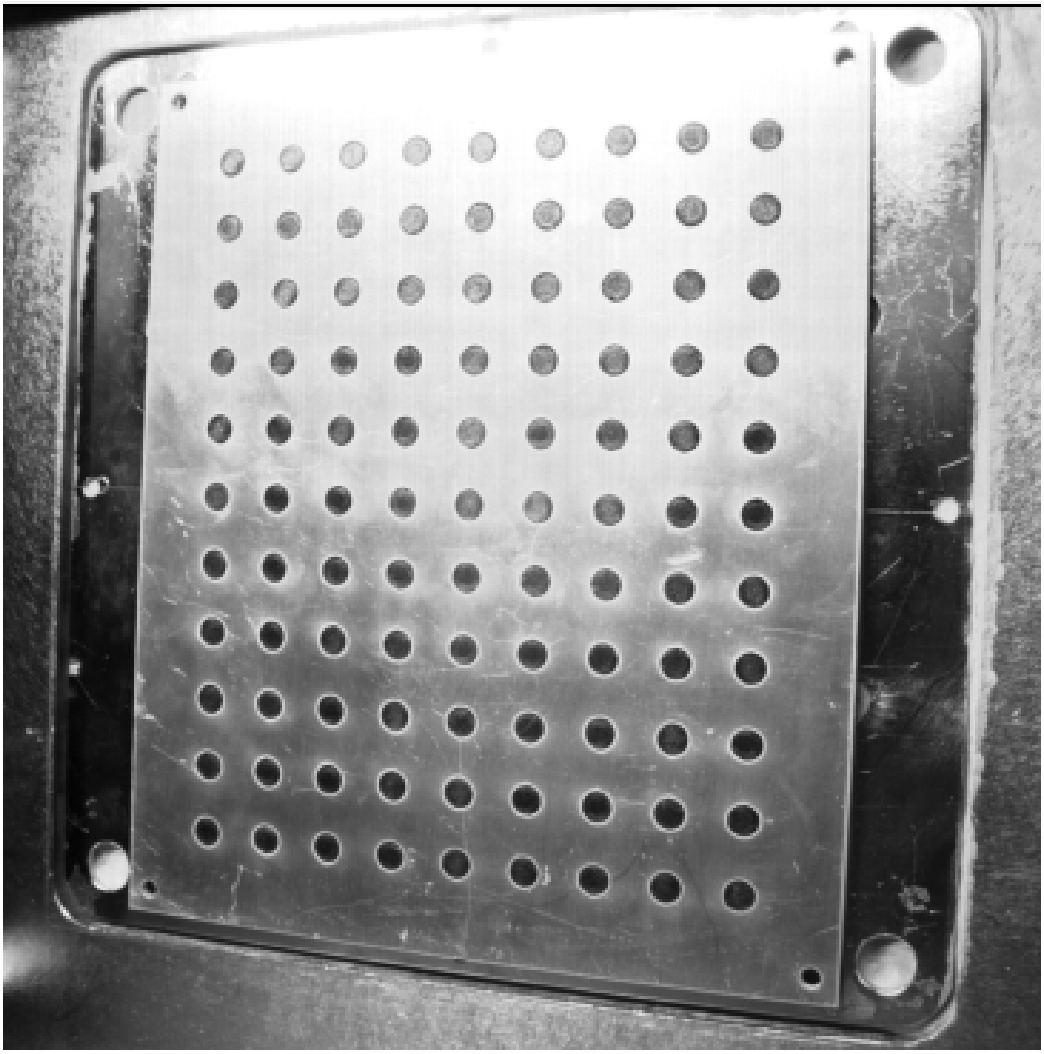


Figure 4.4: Uncorrected NIR image of calibration plate within the FS271M build chamber.

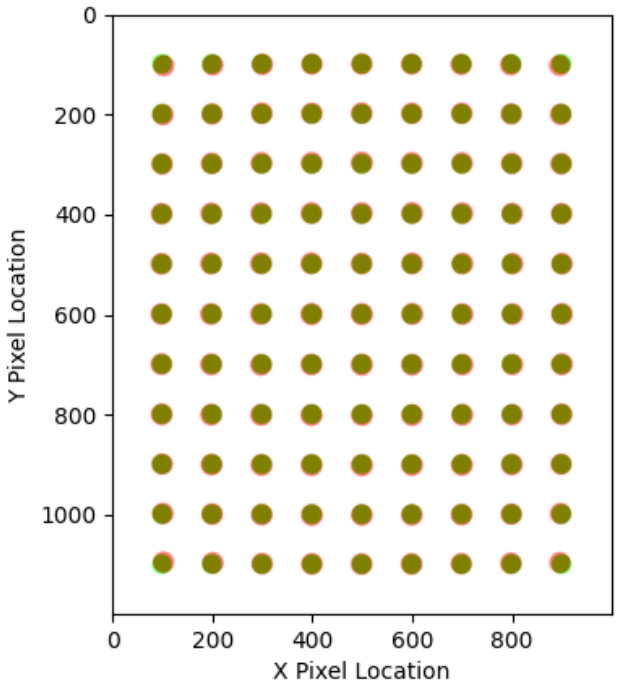


Figure 4.5: Overlayed images of detected of NIR corrected pattern (red) to mathematical-based model of the plate (green).

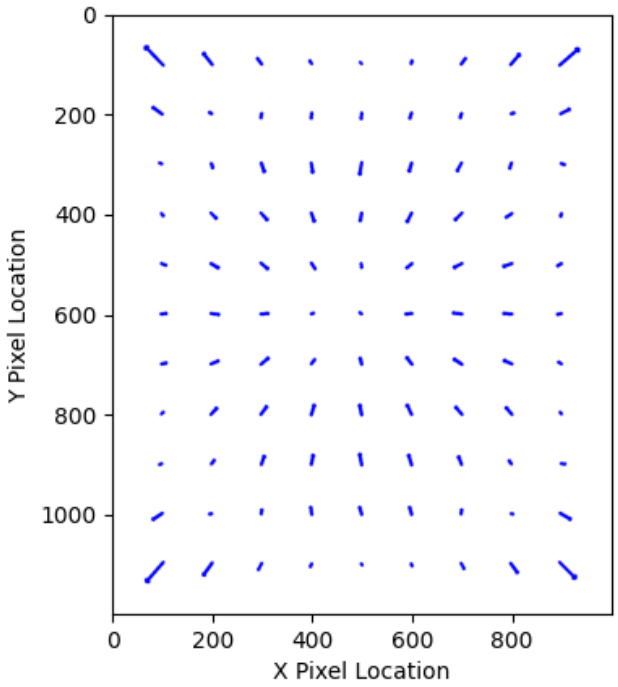


Figure 4.6: NIR image center location difference vector field in pixels (scaled by 10).

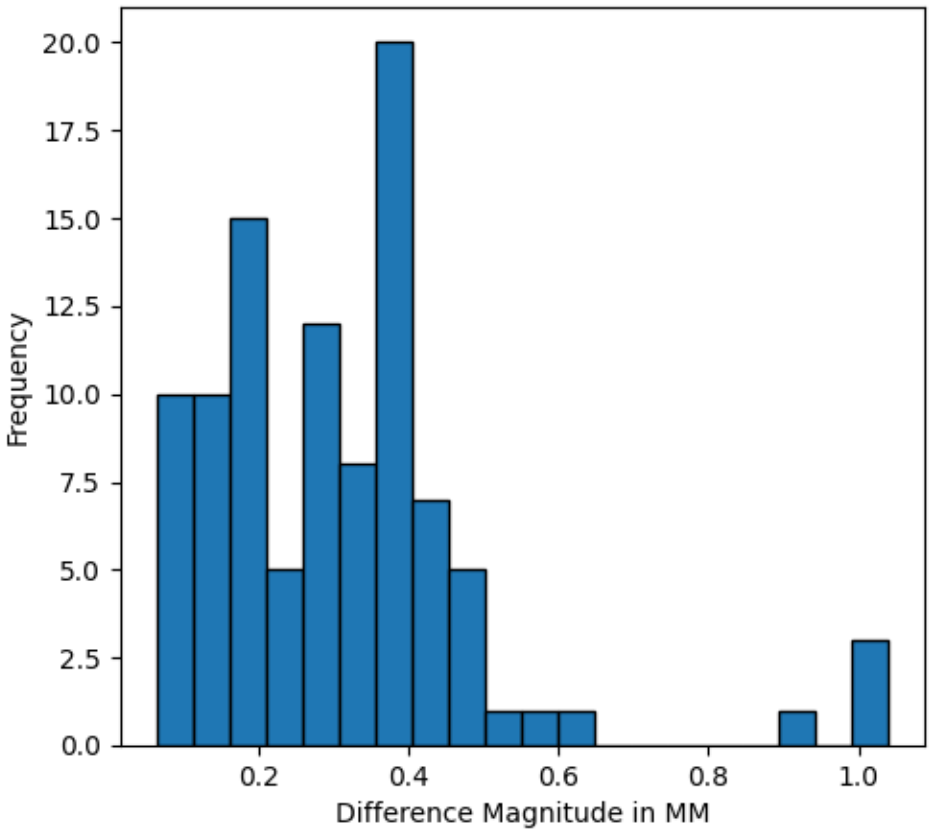


Figure 4.7: Histogram of error magnitudes for NIR.

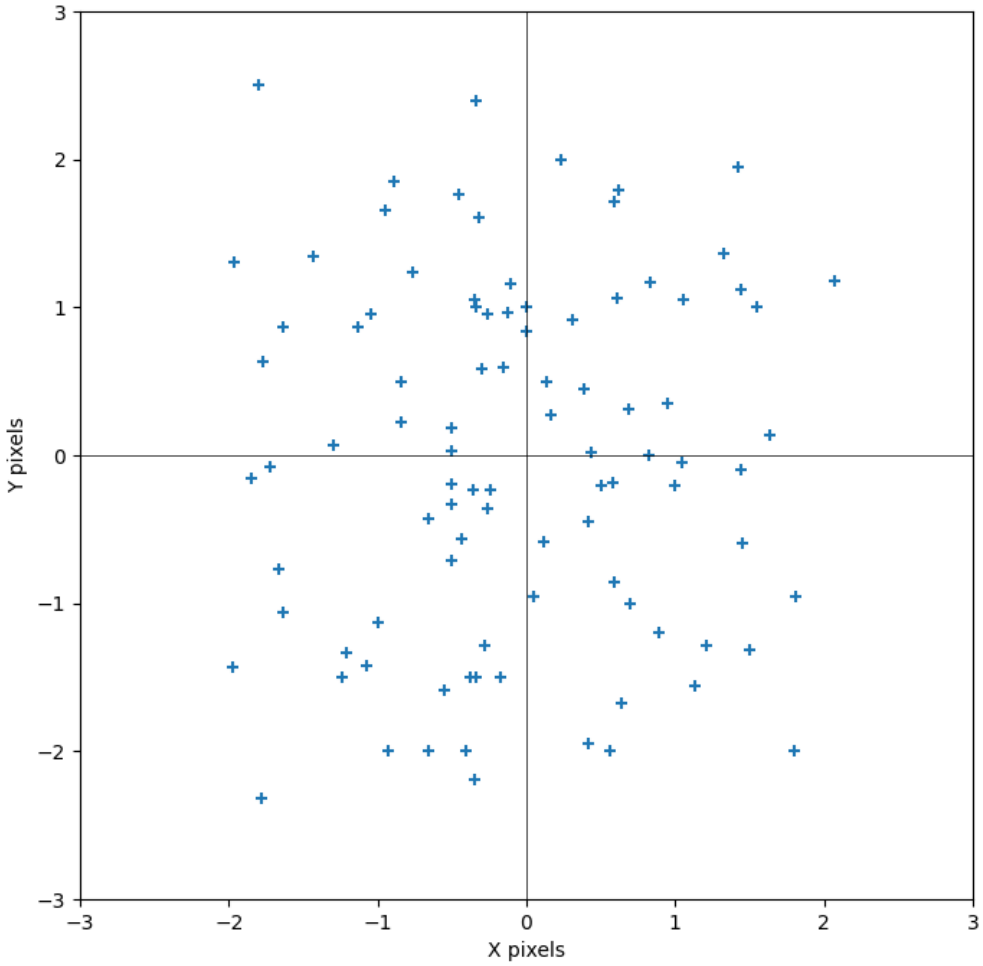


Figure 4.8: Reprojection error of corrected NIR image.

FLIR Results

Given the significantly lower resolution of the FLIR compared to the NIR modality, OpenCV's upscaling involves interpolation. The OpenCV process maps the centers of the source image to the exact centers of the destination image, resulting in zero displacements for all images due to the values being interpolated that are missing. To verify that an error occurs due to upscaling interpolation, an image was generated based on the original FLIR image without upscaling. Instead, a lower resolution was used. The original FLIR image, shown in Figure 4.9, was 640 by 480 pixels and was perspective-corrected to an image of 300 by 350 pixels, a resolution smaller than the native FLIR image. In Figure 4.10, the initial FLIR image (red) was overlaid with the mathematical model of the plate (green). Despite the lower resolution, the image was transformed relatively accurately. Figure 4.11 displays the amplitude of the differences between centers, magnified by a scalar value of 1000 for clarity. The maximum error displacement was 0.0013 mm, with an average error of 0.0012 mm. The distribution of these measurements is shown in Figure 4.12. The reprojection error of the optical transform, which shows a scatter plot of x and y error in pixels of the reprojection error, can be seen in Figure 4.13.

Optical Results

The initial optical image, seen in Figure 4.14 was transformed to a resolution of 1000 by 1200 pixels from an original resolution of 5472 by 3648 pixels. In Figure 4.15, the initial optical image (red in the image) was then overlayed with the mathematical-based model of the plate (green). To determine the accuracy of the transform, the center of the perspective-transformed circles were found and compared to the expected centers of the circle by taking the difference between centers. Figure 4.16 displays the displacement of the differences between centers, magnified by a scalar value of 10 for ease of viewing. Figure 4.16 shows that the error plots follow a pattern expected for aberrations in camera optics. Since this calibration only addresses distortion

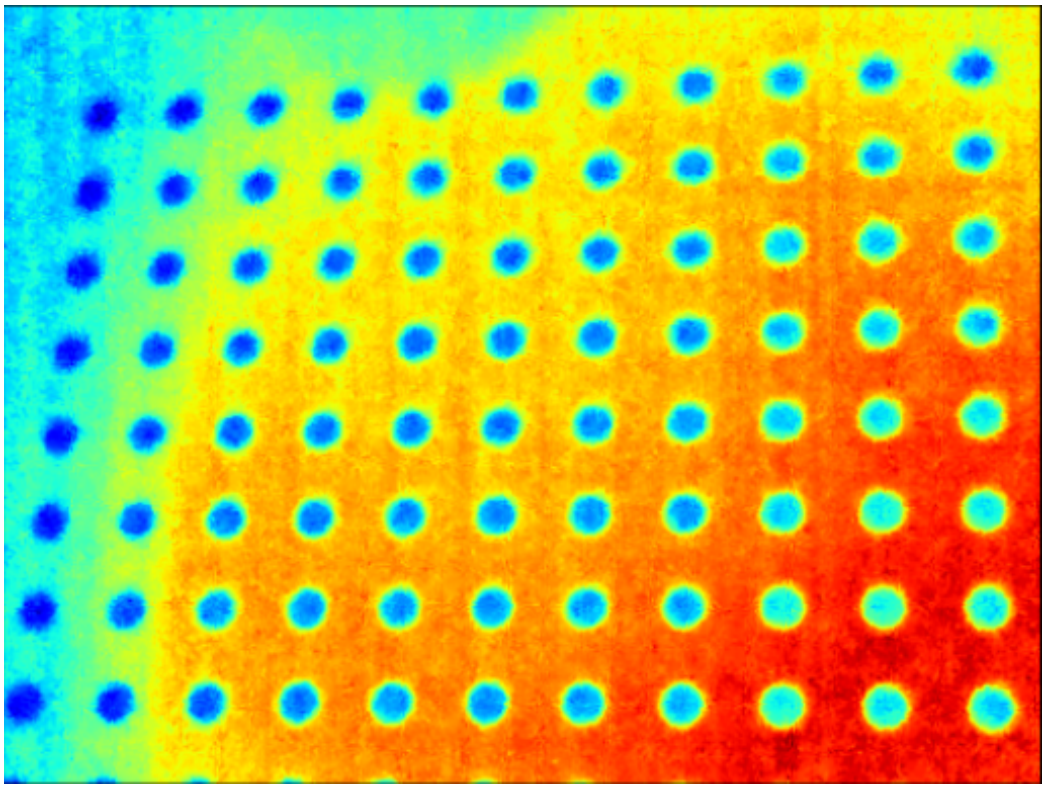


Figure 4.9: Uncorrected FLIR image of calibration plate within the FS271M build chamber.

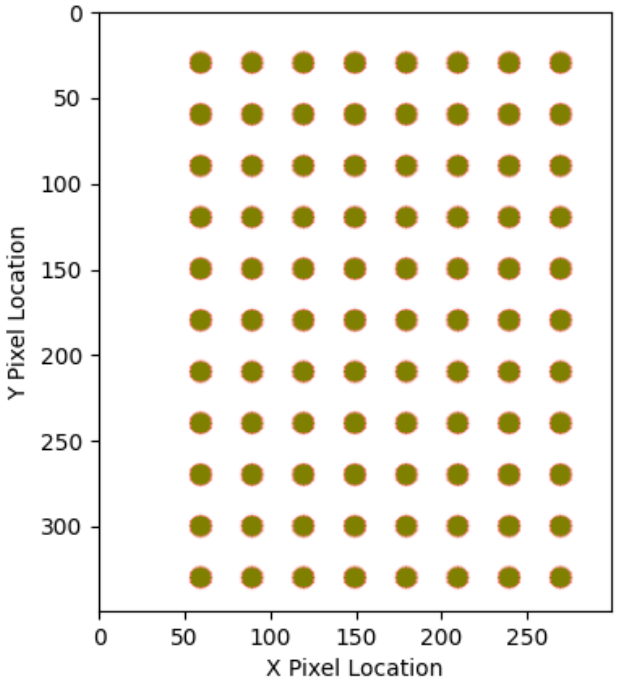


Figure 4.10: Overlayed images of detected of FLIR corrected pattern (red) to mathematical-based model of the plate (green).

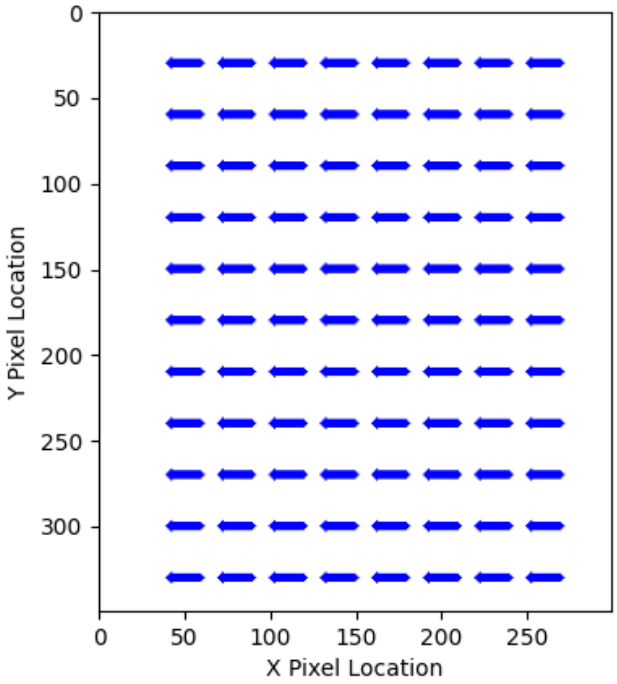


Figure 4.11: FLIR image center location difference vector field plot in pixels (scaled by 1000).

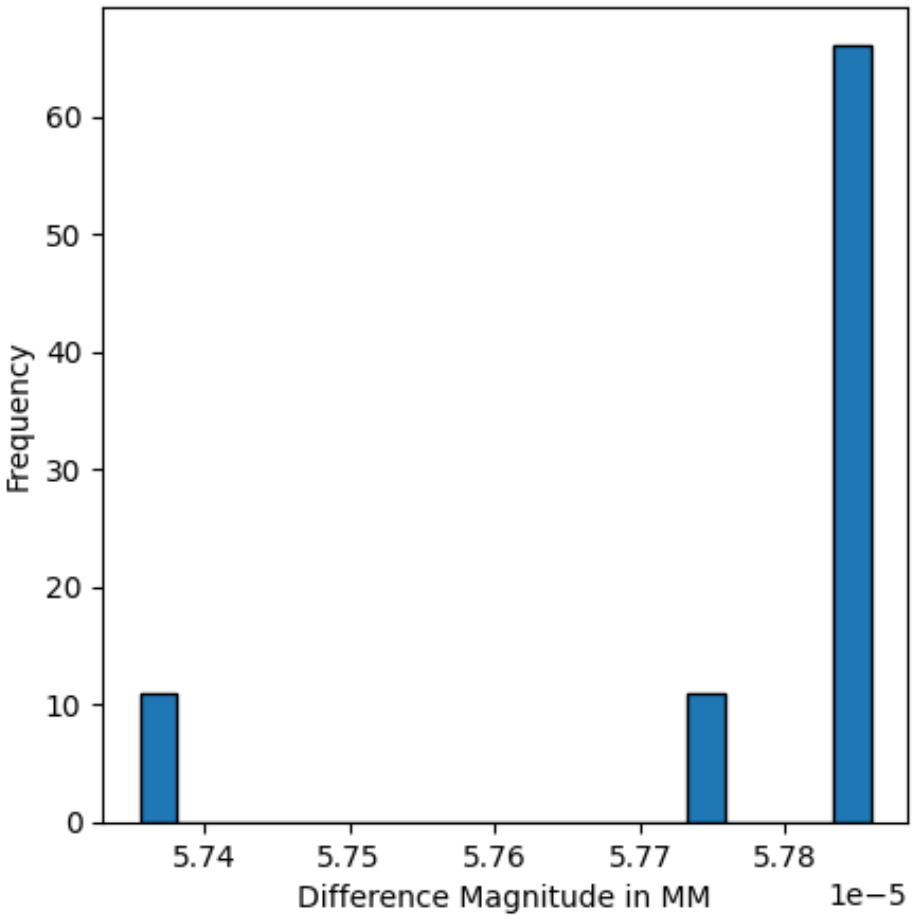


Figure 4.12: Histogram of error magnitudes for FLIR.

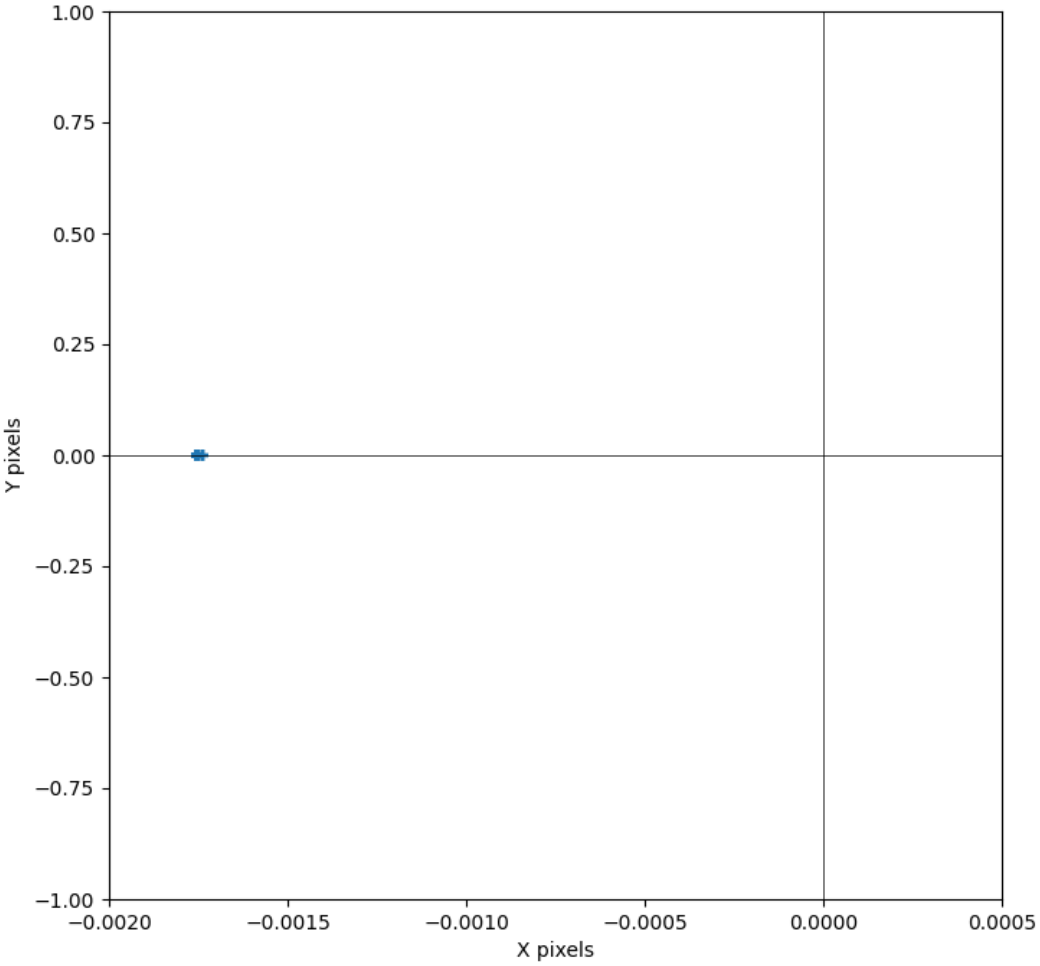


Figure 4.13: Reprojection error of corrected FLIR image.

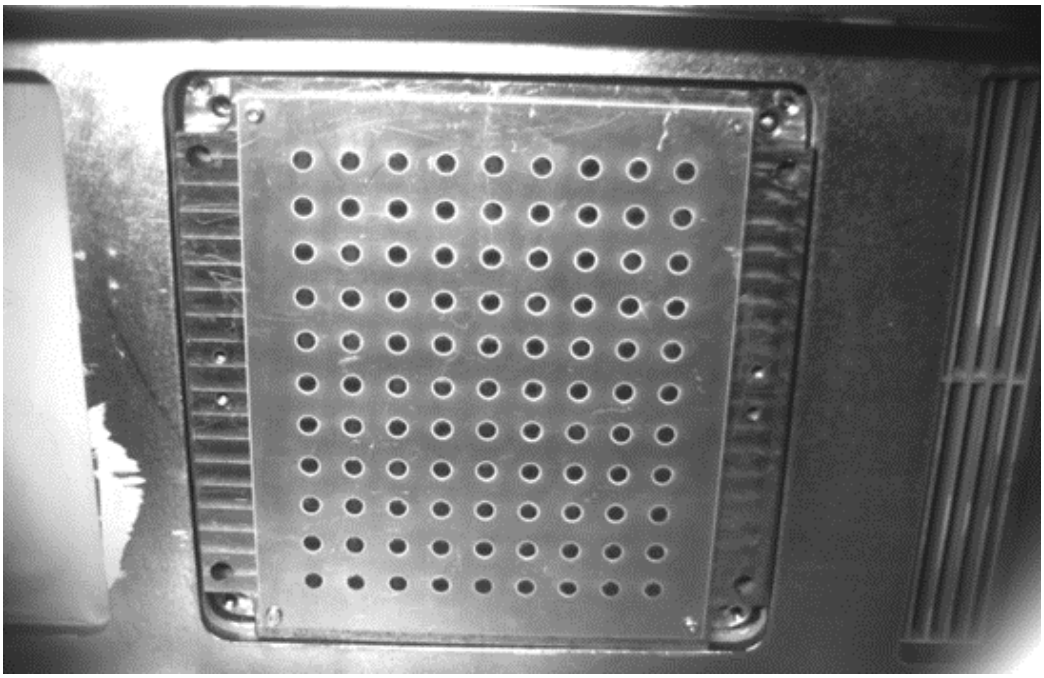


Figure 4.14: Uncorrected optical image of calibration plate within the FS271M build chamber.

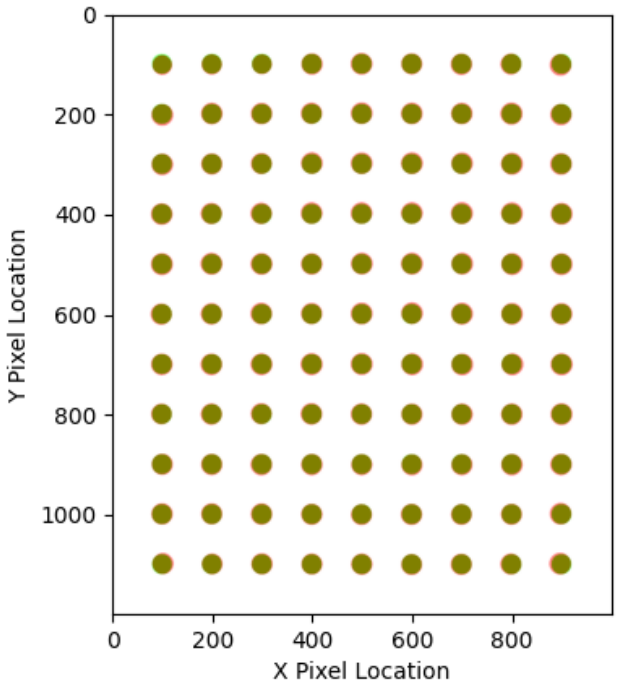


Figure 4.15: Overlayed images of detected optical corrected pattern (red) to mathematical-based model of the plate (green).

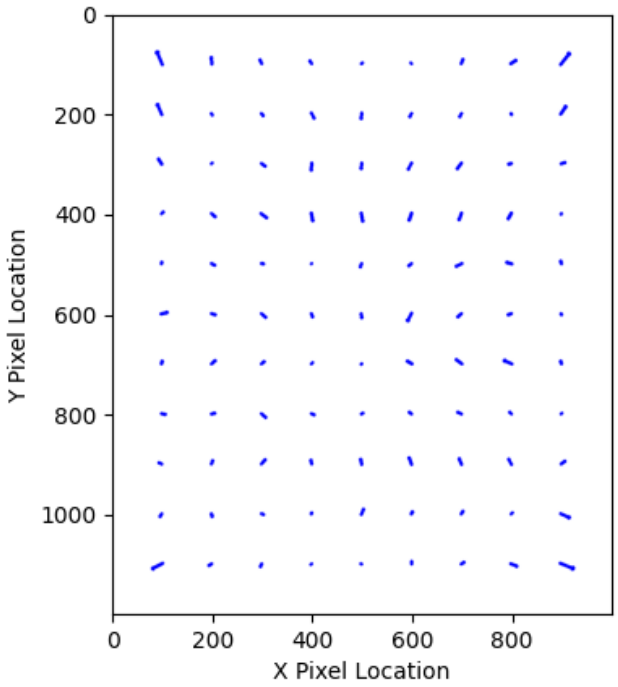


Figure 4.16: Optical image center location difference vector field plot in pixels (scaled by 10).

free images, it is incapable of fully correcting these common optical errors (Choi et al., 2006). The maximum error displacement was 0.575 mm with the average error being 0.199 mm. Figure 4.17 displays the distribution in the measured error. The reprojection error of the optical transform, which shows a scatter plot of x and y error in pixels of the reprojection error, can be seen in Figure 4.18.

4.4.2 Perspective Correction Results

The following figures display the resulting perspective correction on the NIR and FLIR images. The maximum error magnitude for the NIR when performing the perspective correction program results in a max difference value of 1.105 and an average error value of 0.312 mm. When correcting the FLIR image to a size of 300 by 350 pixels, the max difference value was 0.0012 mm and the average value of error was 0.00125 mm for the corrected image to the expected image. For the optical image correction, the maximum error was 0.575mm with an average error was 0.199mm. The final corrected images with scale corrected to a common resolution of 1000 by 1200 can be seen in Figure 4.19.

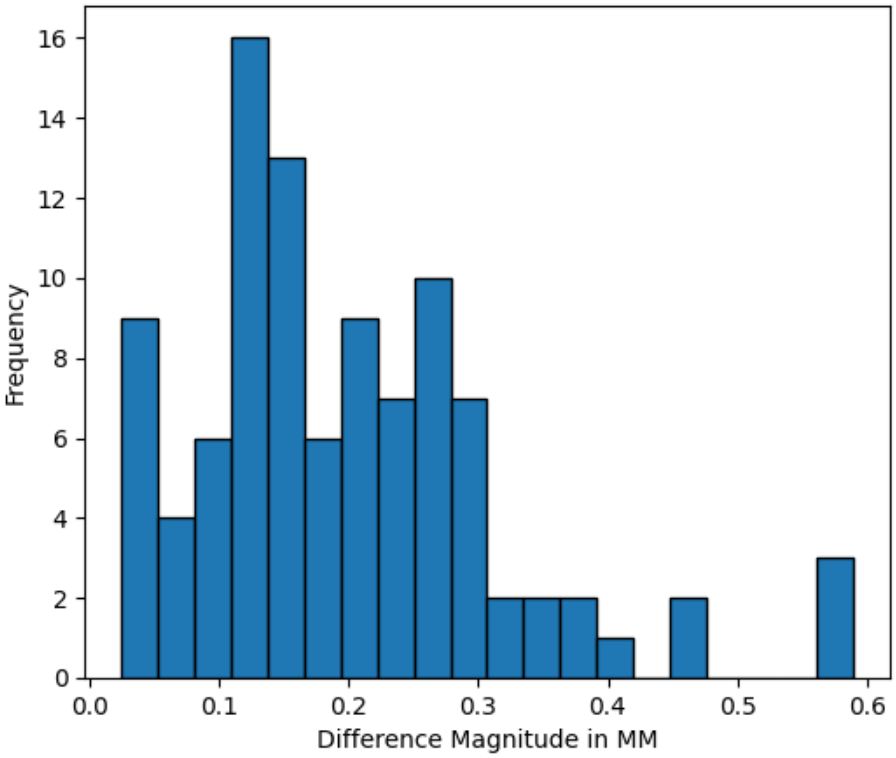


Figure 4.17: Distribution of error magnitudes for optical.

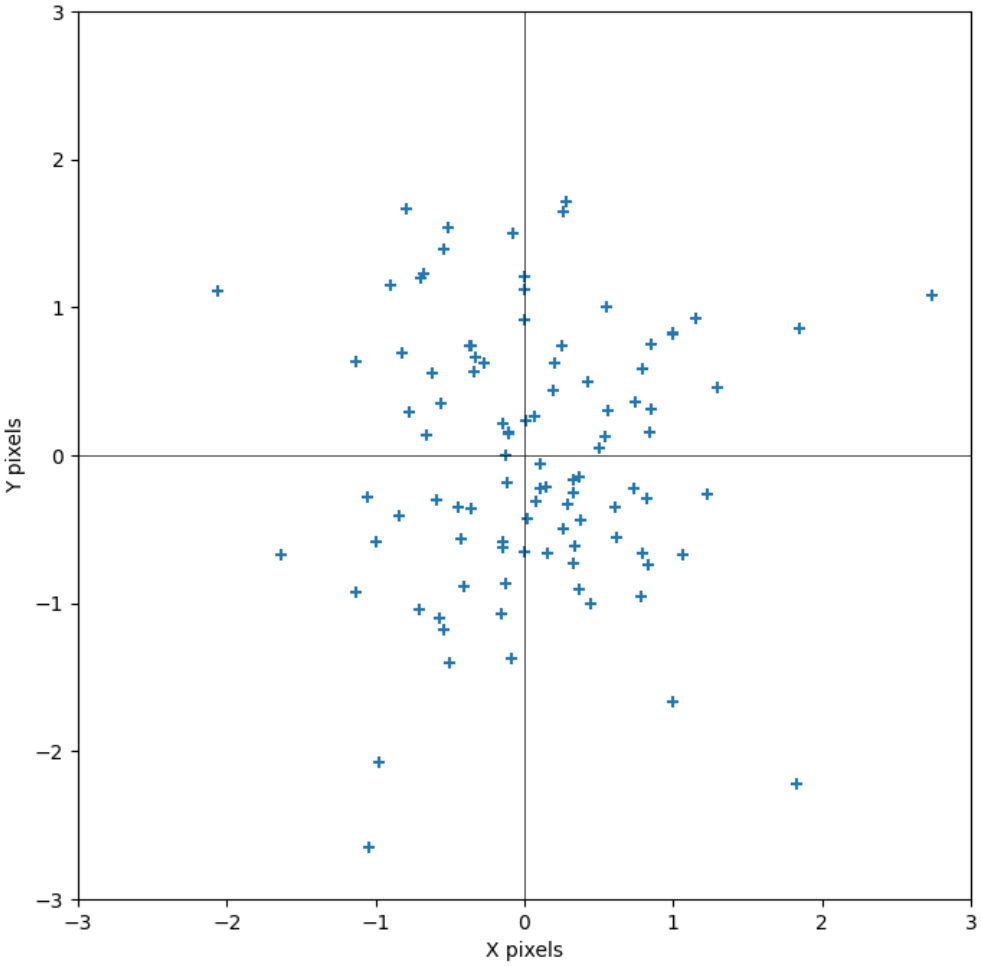
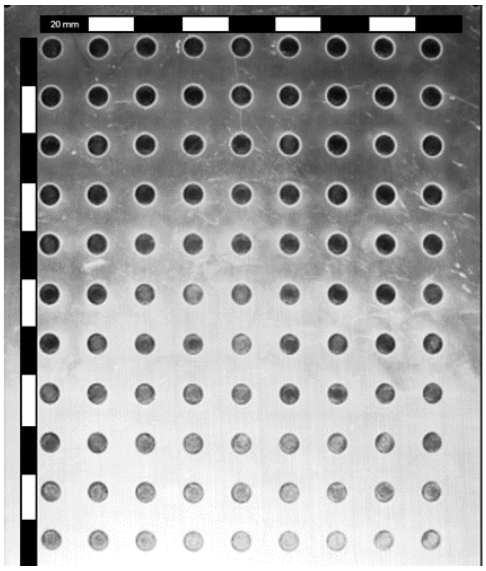
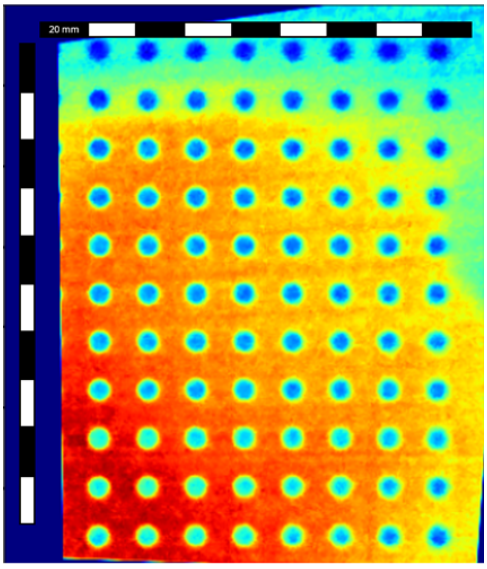


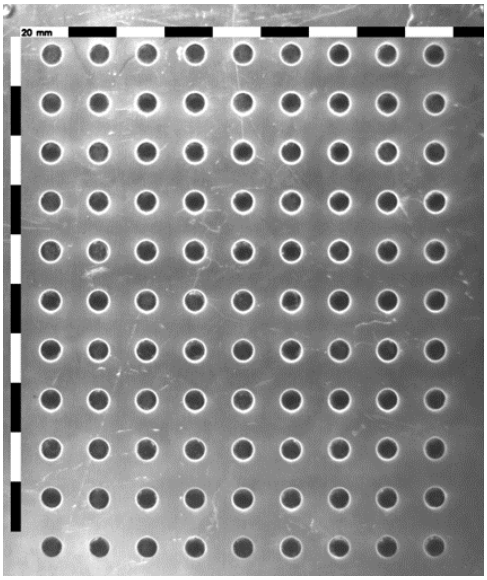
Figure 4.18: Reprojection error of corrected optical image.



(a) NIR Corrected Image.



(b) FLIR Corrected Image.



(c) Optical Corrected Image.

Figure 4.19: Final corrected images after perspective correction

Chapter 5

Data Utilization

5.1 Computer Hardware

A Dell Alienware Aurora R16 serves as the primary computer system for processing tasks. It is equipped with an Intel Core i9-14900KF CPU, which features a 68 MB cache, 24 cores, and can reach a maximum clock speed of 6.0 GHz under P-Core Thermal Velocity Boost. The operating system installed is Windows 11. For graphical processing, the system utilizes an NVIDIA GeForce RTX 4070 Ti SUPER with 16 GB of GDDR6X memory. Additionally, the computer is equipped with 64 GB of DDR5 RAM operating at 5200 MT/s. This specific system retailed at $2,819.99.

5.2 Post-Build Data Processing

5.2.1 Optical Processing

Besides the computer vision algorithm applied to the images via Addiguru, internally optical images are perspective corrected. After perspective correction occurs, multiple filters can be applied to optical images to generate a saliency map. Saliency maps are important for data processing as they enable the identification of key features and patterns within large datasets, thereby improving the efficiency of data analysis.

Filters and the resulting saliency maps can be seen in Figure 5.1. The resulting salinecy maps can be used to identify areas of interest such as non-uniform surfaces, part edges, discoloration, and hatch overlap boundaries. Perspective corrected images of pre-powder spread and post-powder spread images can be found in Figure 5.2 and 5.3. Work is currently on going to correlate areas of interest identified by saliency maps to defects such as swelling and voids found in printed parts.

5.2.2 NIR Processing

As discussed in Section 3.2.2, layer images are created using 'numpy.max'. After the 'numpy.max' function is applied, perspective transform is applied. This results in a layer wise image that shows intensity levels that are related to the energy input into the powder-bed can be seen in Figure 5.4. Volumetric reconstruction has been conducted using these results and future work will be looking more into the relation of measured intensity levels to observable defects such as correlating hot spots to defects like spatter, lack of fusion, and subsurface flaws.

5.2.3 IR Processing

All data processing is conducted before applying the perspective transform to obtain processed results, such as identifying interpass temperature and temperature gradients. The identification of interpass temperature and the computation of temperature gradients, both spatially and temporally, are key components of detecting defects. Temporal gradients are determined by taking the difference between consecutive frames and dividing by the time step between images. Spatial gradients are calculated using the 'numpy.gradient' function, which employs second-order accurate central differences for interior points, and either first or second-order accurate one-sided (forward or backward) differences at the boundaries Harris et al. (2020). Resulting temporal and spatial temperature gradients can be seen in Figure

5.6 and 5.7, respectively. These images can be used in correlating defects such as porosity and cracking.

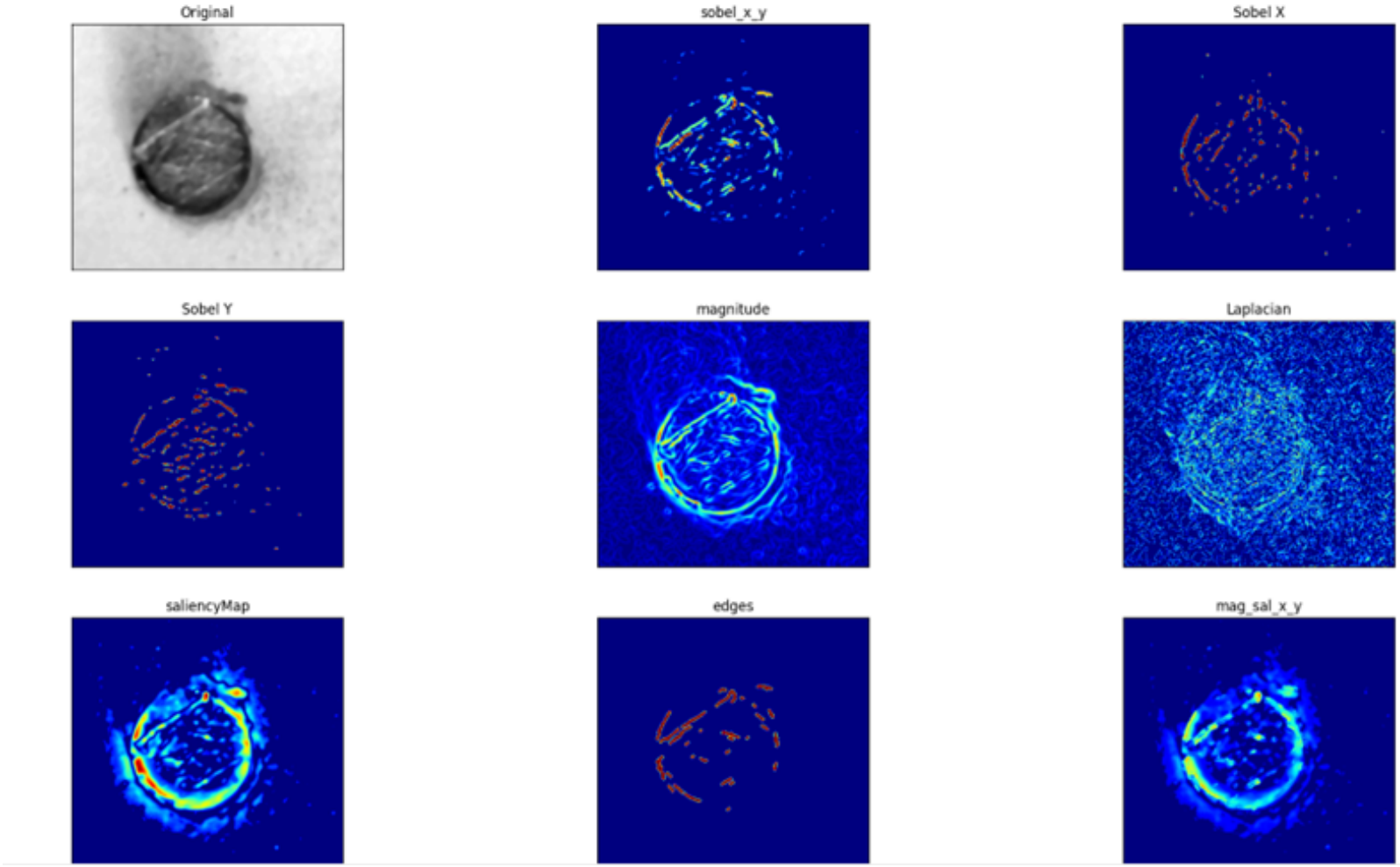


Figure 5.1: Optical saliency maps showing potential areas of interest.

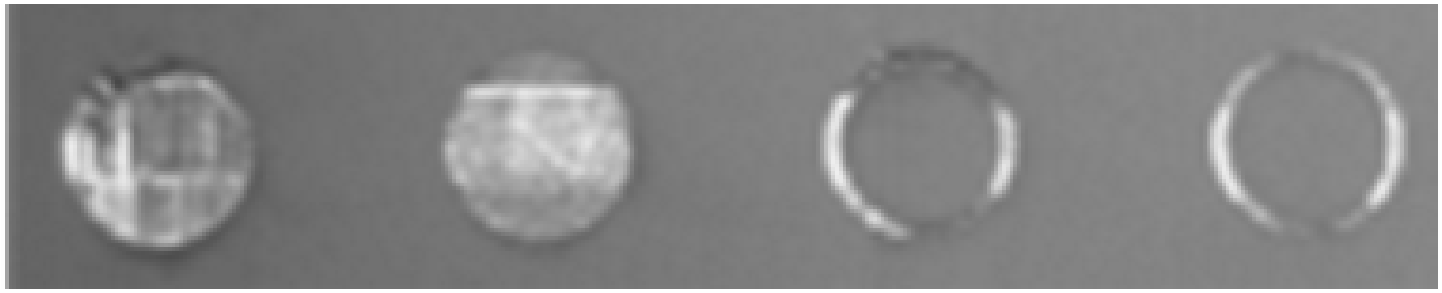


Figure 5.2: Example of pre-powder optical image.

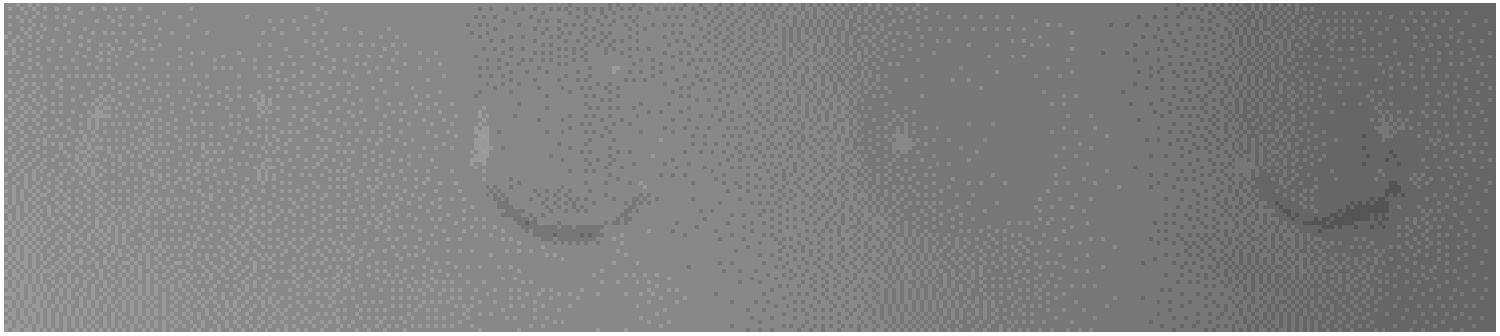


Figure 5.3: Example of post-powder optical image.

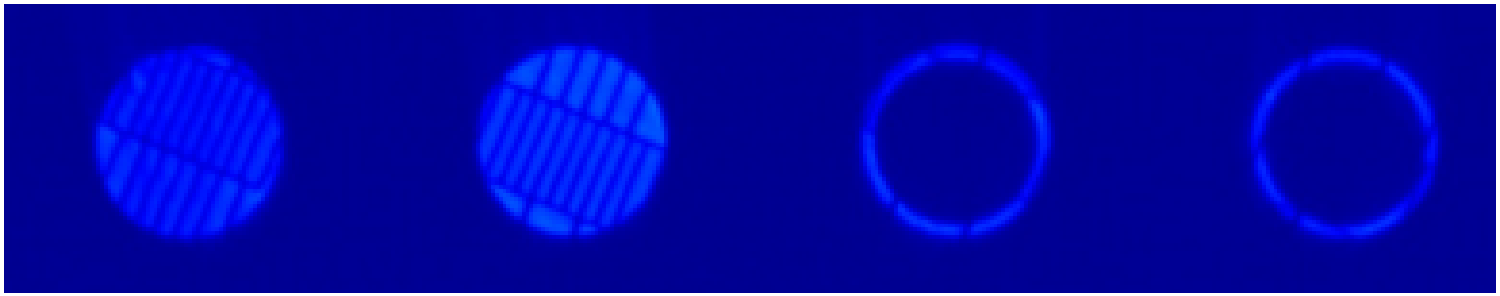


Figure 5.4: Example of layer-wise NIR image.

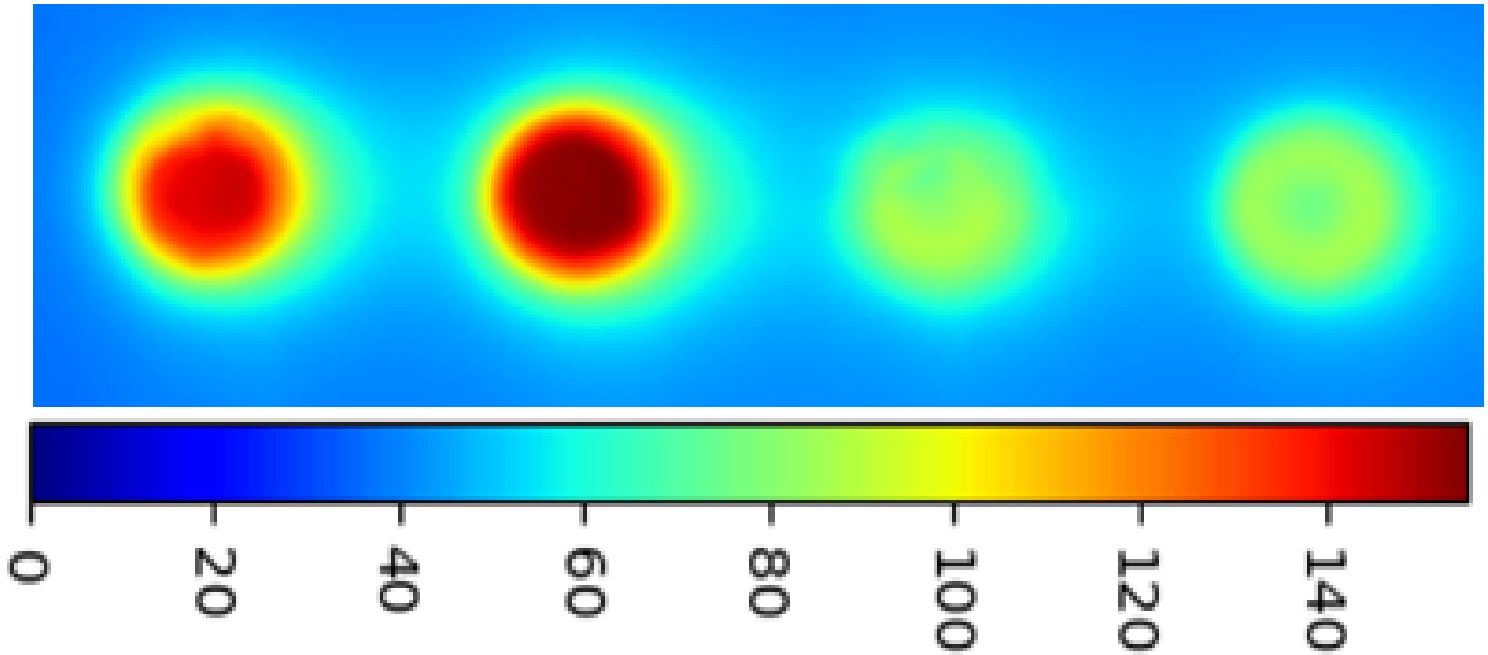


Figure 5.5: Example of IR interpass temperature.

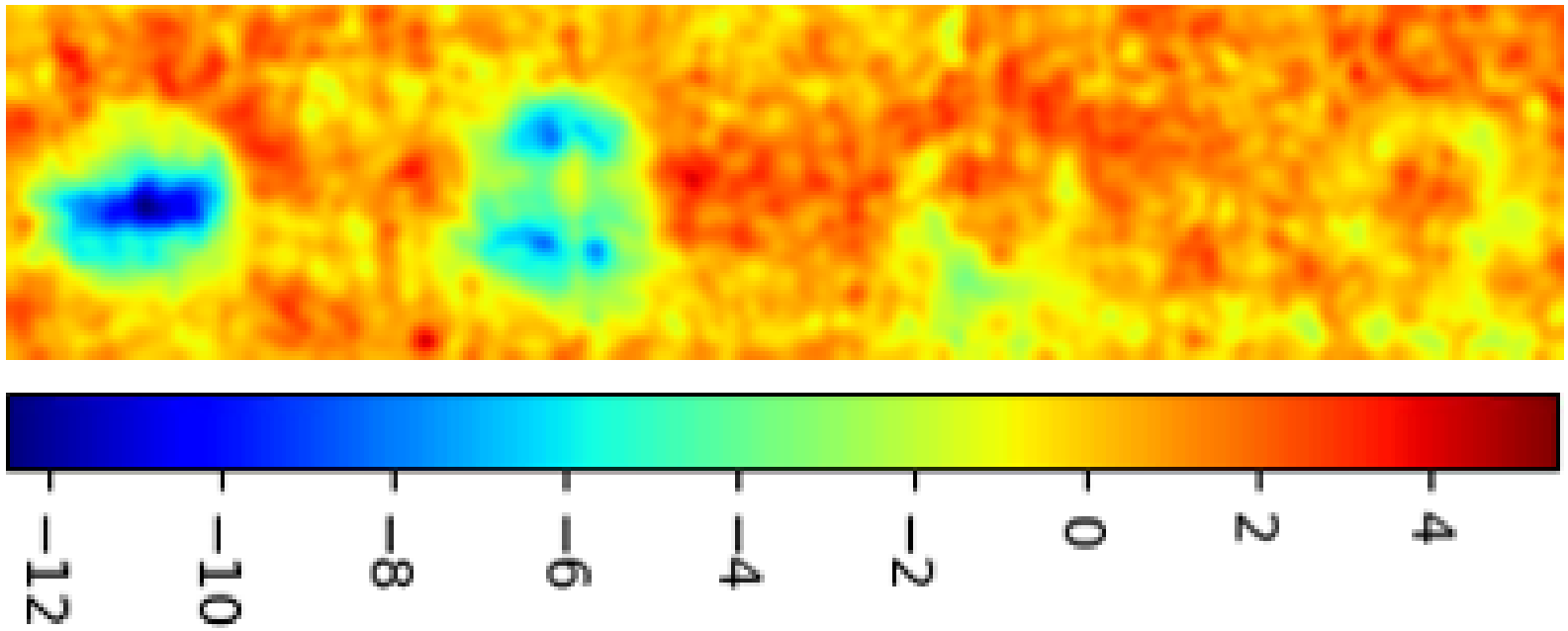


Figure 5.6: Example of IR temporal temperature gradient °C/s.

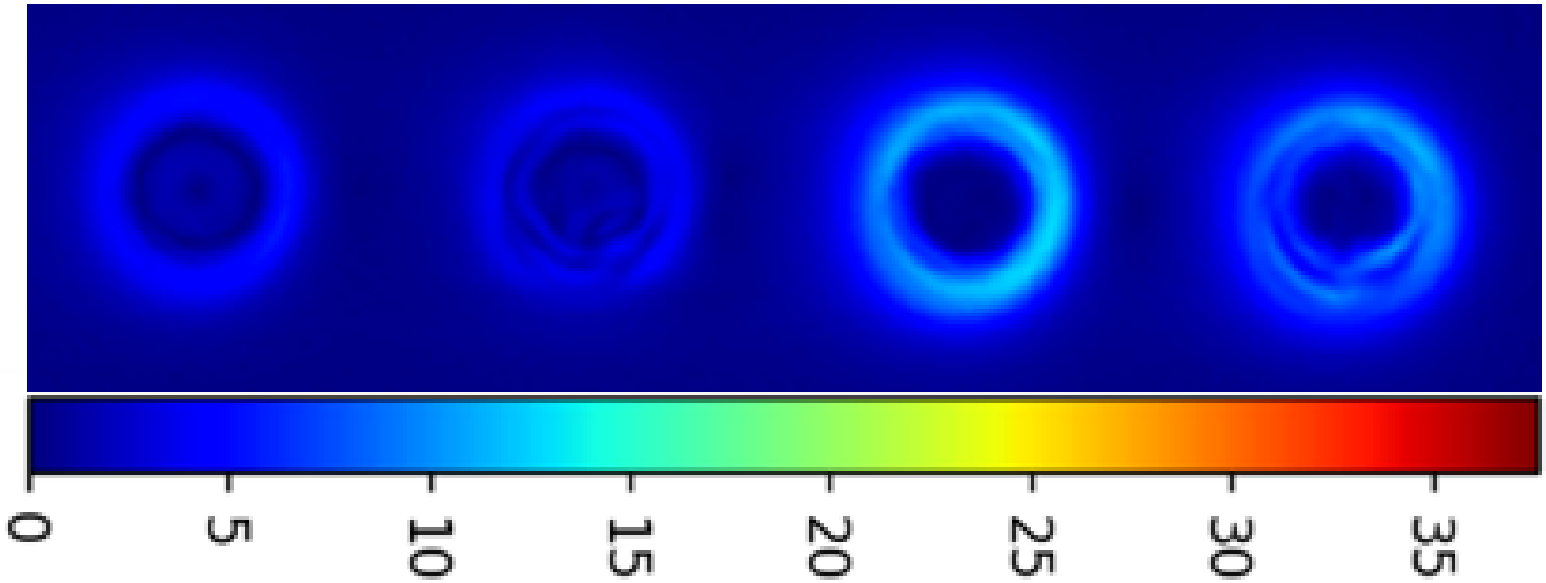


Figure 5.7: Example of IR spatial temperature gradient °C/pixel

Chapter 6

Conclusions

In conclusion, developed is a comprehensive, low-cost image collection and compilation system for enhanced in-situ monitoring of the Laser-Powder Bed Fusion (L-PBF) process. The use of optical, near-infrared (NIR), and infrared (IR) cameras, along with a low-cost, custom-designed calibration plate, has enabled precise perspective correction.

The custom calibration plate, designed in a symmetric circular grid pattern, facilitated the alignment of images from different cameras, thereby ensuring consistent and reliable data across various imaging modalities. This advancement addresses a critical challenge in the field of additive manufacturing: the need for high-precision, multi-angle defect detection within the constrained physical dimensions of an L-PBF machine.

The Python-based data acquisition system developed for this research has proven to be efficient and capable of handling the demands of real-time monitoring. The system's ability to operate independently of the L-PBF machine and its use of the HDF5 format for data storage, ensure that large volumes of data can be managed effectively. Pixelink and Spinnaker API's allow for future capability of in-situ Python analysis. This setup allows for detailed analysis and long-term storage, which are crucial for continuous improvement and quality assurance in manufacturing processes.

Furthermore, this low-cost solution offers significant potential for scalability and adaptability across different build environments. The methodology and technology developed in this thesis can be implemented in various L-PBF systems, making it a versatile tool for quality assurance in additive manufacturing. The cost-effectiveness of the system ensures that high-quality monitoring is accessible to a broader range of users, from small research labs to large-scale industrial operations.

Future work will focus on further refining the system to enhance its real-time processing capabilities and exploring the potential use of more imaging cameras to capture a wider range of defects. Optimizing the ROI of recording areas is also needed as this will reduce the image size and FOT for NIR images. These advancements will further improve the robustness and reliability of the system.

Bibliography

AbouelNour, Y. and Gupta, N. (2023). Assisted defect detection by in-process monitoring of additive manufacturing using optical imaging and infrared thermography. *Additive Manufacturing*, 67:103483. 9

Addiguru (2024). Lpbf process. 3, 13

Alldredge, J., Slotwinski, J., Storck, S., Kim, S., Goldberg, A., and Montalbano, T. (2018). In-situ monitoring and modeling of metal additive manufacturing powder bed fusion. In *AIP Conference Proceedings*, volume 1949, pages 020007–1–020007–8. AIP Publishing. 4

Ashby, e. a. (2022). Thermal analysis of parts produced by l-pbf and correlation with dimensional accuracy. *Thermal Science and Engineering Progress*, 27:101101. 9

Bartlett, J., Heim, F., Murty, Y., and Li, X. (2018). In situ defect detection in selective laser melting via full-field infrared thermography. *Additive Manufacturing*, 24:595–605. 4

Basler (2024). Basler aca5472-17um camera. 12

Baumgartl, H., Tomas, J., Buettner, R., and Merkel, M. (2020). A deep learning-based model for defect detection in laser-powder bed fusion using in-situ thermographic monitoring. *Progress in Additive Manufacturing*, 5:277–285. 9

Bradski, G. (2000). The opencv library. *Dr. Dobb's Journal of Software Tools*. xi, 41, 42

Choi, K. S., Lam, E. Y., and Wong, K. K. Y. (2006). Automatic source camera identification using the intrinsic lens radial distortion. *Optics Express*, 14:11551–11565. 47, 62

Craeghs, T., Clijsters, S., Kruth, J.-P., Bechmann, F., and Ebert, M. C. (2012). Detection of process failures in layerwise laser melting with optical process monitoring. *Physics Procedia*, 39:753–759. 3

Deckers, T., Wolf, F., Forêt, P., Witt, G., and Kleszczynski, S. (2023). Comparative analysis of process stability in pbf-lb/m: (thermal) highspeed imaging vs. melt pool monitoring using novel gas mixtures. In *Solid Freeform Fabrication 2023: Proceedings of the 34th Annual International Solid Freeform Fabrication Symposium – An Additive Manufacturing Conference*, Duisburg-Essen, Germany. University of Duisburg-Essen. 9

Doubenskaia, M. A., Zhirnov, I. V., Teleshevskiy, V. I., Bertrand, P., and Smurov, I. Y. (2015). Determination of true temperature in selective laser melting of metal powder using infrared camera. *Materials Science Forum*, 834:93–102. 4

ElSheikh, A., Abu-Nabah, B., Hamdan, M., and Tian, G.-Y. (2023). Infrared camera geometric calibration: A review and a precise thermal radiation checkerboard target. *Sensors*, 23(7):3479. 5

Elwarfalli, Papazoglou, E. D. S. (2020). In situ process monitoring for laser-powder bed fusion using convolutional neural networks and infrared tomography. In *Proceedings of the IEEE Conference*. IEEE. 4

EOS (2024). Software plans features comparison. `https://www.eos.info/04_consulting_service_software/software/pdf_software/eos_plans_features_comparison.pdf`. Accessed: 2024-07-13. 16

Estalaki, S. M., Lough, C. S., Landers, R. G., Kinzel, E. C., and Luo, T. (2022). Predicting defects in laser powder bed fusion using in-situ thermal imaging data and machine learning. *Additive Manufacturing*, 58:103008. 9

Farsoon-Technologies (2020). *Farsoon FS271M Product Brochure*. 10

FLIR (2024a). Flir a50/a70 smart sensor. 13

FLIR (2024b). Researchir software capabilities. `https://flir.custhelp.com/app/answers/detail/a_id/3000/related/1`. Accessed: 2024-07-13. 15

FLIR-Systems (2024). Flir cameras - temperature measurement formula. `https://flir.custhelp.com/app/answers/detail/a_id/3321/~/flir-cameras---temperature-measurement-formula`. Accessed: 2024-07-16. 36

Forien, J., Calta, N., DePond, P., Guss, G., Roehling, T., and Matthews, M. (2020). Detecting keyhole pore defects and monitoring process signatures during laser powder bed fusion: a correlation between in situ pyrometry and ex situ x-ray radiography. *Additive Manufacturing*, 35:101336. 4

Foster, S., Carver, K., Dinwiddie, R., et al. (2018). Process-defect-structure-property correlations during laser powder bed fusion of alloy 718: Role of in situ and ex situ characterizations. *Metallurgical and Materials Transactions A*, 49:5775–5798. 9

Fournet-Fayard, L., Cayron, C., Koutiri, I., Lapouge, P., Guy, J., Dupuy, C., and Obaton, A.-F. (2023). Thermal analysis of parts produced by l-pbf and correlation with dimensional accuracy. *Welding in the World*, 67:845–858. 9

Gaikwad, A., Imani, F., Yang, H., Reutzel, E., and Rao, P. (2019). In situ monitoring of thin-wall build quality in laser powder bed fusion using deep learning. *Smart and Sustainable Manufacturing Systems*, 3(1). 3

Gong, H., Rafi, K., Gu, H., Starr, T., and Stucker, B. (2014). Analysis of defect generation in ti-6al-4v parts made using powder bed fusion additive manufacturing processes. *Additive Manufacturing*, 1:87–98. 4

Gordon, J., Narra, S., Cunningham, R., Liu, H., Chen, H., Suter, R., Beuth, J., and Rollett, A. (2020). Defect structure process maps for laser powder bed fusion additive manufacturing. *Additive Manufacturing*, 36:101552. 4

Gunenthiram, V., Montazeri, M., Peyre, P., Schneider, M., Ji, H., and Carin, M. (2018). Investigating spatter and plume in metal additive manufacturing using laser powder bed fusion. *Journal of Materials Processing Technology*, 252:602–613. 4

Gzip-Project (2024). Gzip. `https://www.gzip.org/`. Accessed: 2024-07-13. 37

Harris, C. R., Millman, K. J., van der Walt, S. J., Gommers, R., Virtanen, P., Cournapeau, D., Wieser, E., Taylor, J., Berg, S., Smith, N. J., Kern, R., Picus, M., Hoyer, S., van Kerkwijk, M. H., Brett, M., Haldane, A., del Río, J. F., Wiebe, M., Peterson, P., Gérard-Marchant, P., Sheppard, K., Reddy, T., Weckesser, W., Abbasi, H., Gohlke, C., and Oliphant, T. E. (2020). Array programming with NumPy. *Nature*, 585(7825):357–362. 67

Khairallah, S. A., Anderson, A. T., Rubenchik, A. M., and King, W. E. (2016). First observation of the plume and spatter formation in laser powder bed fusion. *Acta Materialia*, 108:36–45. 4

King, W., Barth, H., Castillo, V., Gallegos, G., Gibbs, J., Hahn, D., Kamath, C., and Rubenchik, A. (2014). Observation of keyhole-mode laser melting in laser powder-bed fusion additive manufacturing. *Journal of Materials Processing Technology*, 214:2915–2925. 4

Land, W. S., Zhang, B., Ziegert, J., and Davies, A. (2015). In-situ metrology system for laser powder bed fusion additive process. *Procedia Manufacturing*, 1:393–403. 3

Lane, B., Moylan, S., Whitenton, E. P., and Ma, L. (2016). Thermographic measurements of the commercial laser powder bed fusion process at nist. *Rapid Prototyping Journal*, 22(5):778–787. 4

Liu, T., Lough, C. S., Sehhat, H., Ren, Y. M., Christofides, P. D., Kinzel, E. C., and Leu, M. C. (2022). In-situ infrared thermographic inspection for local powder layer thickness measurement in laser powder bed fusion. *Additive Manufacturing*, 55:102873. 9

Lough, C. S., Liu, T., Wang, X., Brown, B., Landers, R. G., Bristow, D. A., Drallmeier, J. A., and Kinzel, E. C. (2022). Local prediction of laser powder bed fusion porosity by short-wave infrared imaging thermal feature porosity probability maps. *Journal of Materials Processing Technology*, 302:117473. 4, 9

McNeil, J. L., Sisco, K., Frederick, C., Massey, M., Carver, K., List, F. I., Qiu, C., Mader, M., Sundarraj, S., and Babu, S. (2020). In-situ monitoring for defect identification in nickel alloy complex geometries fabricated by l-pbf additive manufacturing. *Metallurgical and Materials Transactions A*, 51(12):6528–6545. 4, 5

Mireles, J., Ridwan, S., Morton, P., Hinojos, A., and Wicker, R. (2015). Analysis and correction of defects within parts fabricated using powder bed fusion technology. *Surface Topography: Metrology and Properties*, 3:034002. 4

Mohr, G., Altenburg, S. J., and Hilgenberg, K. (2020a). Effects of inter layer time and build height on resulting properties of 316l stainless steel processed by laser powder bed fusion. *Additive Manufacturing*, 32:101080. 4

Mohr, G., Nowakowski, S., Altenburg, S. J., Maierhofer, C., and Hilgenberg, K. (2020b). Experimental determination of the emissivity of powder layers and bulk material in laser powder bed fusion using infrared thermography and thermocouples. *Metals*, 10(11):1546. 9

Mohr, G., Scheuschner, N., and Hilgenberg, K. (2020c). In situ heat accumulation by geometrical features obstructing heat flux and by reduced inter layer times in laser powder bed fusion of aisi 316l stainless steel. *Procedia CIRP*, 94:155–160. 4, 6

Nguyen, N. V., Hum, A. J. W., Do, T., and Tran, T. (2023). Semi-supervised machine learning of optical in-situ monitoring data for anomaly detection in laser powder bed fusion. *Virtual and Physical Prototyping*, 18(1):e2129396. 3

Patel, M., Malekipour, E., Pallikonda, V., and Jain, P. (2020). Review of process parameters influencing laser polishing of additive manufactured metals and alloys. *Optics & Laser Technology*, 131:106439. 4

Pixelink (2024a). Pixelink python wrapper. Accessed: 2024-07-20. 13

Pixelink (2024b). *PL-D734 Camera Datasheet*. Accessed: 2024-07-12. x, 8, 12

Pixelink Support (2024). Pl-d732/734 readout timing. Accessed: 2024-07-16. 33

Plotnikov, Y., Henkel, D., Burdick, J., French, A., Sions, J., and Bourne, K. (2019). Infrared-assisted acoustic emission process monitoring for additive manufacturing. In *AIP Conference Proceedings*, volume 2102, page 020006. AIP Publishing. 9

Promoppatum, P., Srinivasan, R., Quek, S., Msolli, S., Shukla, S., Johan, N., van der Veen, S., and Jhon, M. (2022). Quantification and prediction of lack-of-fusion porosity in the high porosity regime during laser powder bed fusion of ti-6al-4v. *Journal of Materials Processing Technology*, 300:117426. 4

Raplee, J., Gockel, J., List, F., et al. (2020). Towards process consistency and in-situ evaluation of porosity during laser powder bed additive manufacturing. *Science and Technology of Welding and Joining*, 25(8):679–689. 9

Raplee, J., Plotkowski, A., Kirka, M. M., Dinwiddie, R., Okello, A., Dehoff, R. R., and Babu, S. S. (2017). Thermographic microstructure monitoring in electron beam additive manufacturing. *Scientific Reports*, 7:43554. 9

Ridwan, S., Mireles, J., Gaytan, S., Espalin, D., and Wicker, R. (2014). Automatic layerwise acquisition of thermal and geometric data of the electron beam melting process using infrared thermography. Master's thesis, University of Texas at Austin. Presented at the 2014 International Solid Freeform Fabrication Symposium. 9

Rieder, H., Holzer, C., Prantl, M., Waser, R., and Holzmann, A. (2020). A deep learning-based model for defect detection in laser-powder bed fusion using in-situ thermographic monitoring. *Progress in Additive Manufacturing*, 5:277–284. 4

Scarpitti, A. and Tocci, E. L. (2021). A preliminary study on the prediction of as-built surface quality in complex l-pbf parts using thermal imaging-based in-situ monitoring. Master's thesis, Politecnico di Milano. Tesi di Laurea Magistrale in Management Engineering, Ingegneria Gestionale. 9

Schwerz, C., Raza, A., Lei, X., Nyborg, L., Hryha, E., and Wirdelius, H. (2021). In-situ detection of redeposited spatter and its influence on the formation of internal flaws in laser powder bed fusion. *Additive Manufacturing*, 47:102370. 3

Scime, L. and Beuth, J. (2018). A multi-scale convolutional neural network for autonomous anomaly detection and classification in a laser powder bed fusion additive manufacturing process. *Additive Manufacturing*, 24:273–286. 3

Scime, L., Siddel, D., Baird, S., and Paquit, V. (2020). Layer-wise anomaly detection and classification for powder bed additive manufacturing processes:

A machine-agnostic algorithm for real-time pixel-wise semantic segmentation. *Additive Manufacturing*, 36:101453. 9

Snow, Z., Scime, L., Ziabari, A., Fisher, B., and Paquit, V. (2023a). Observation of spatter-induced stochastic lack-of-fusion in laser powder bed fusion using in situ process monitoring. *Additive Manufacturing*, 61:103298. 3

Snow, Z., Scime, L., Ziabari, A., Fisher, B., and Paquit, V. (2023b). Scalable in situ non-destructive evaluation of additively manufactured components using process monitoring, sensor fusion, and machine learning. *Additive Manufacturing*, 78:103817. 3

Systems, F. (2024). Spinnaker sdk. `https://www.flir.com/products/spinnaker-sdk/?vertical=machine+vision&segment=iis`. Accessed: 2024-07-20. 15

The HDF Group (2024). Hierarchical Data Format, version 5. 36

Usamentiaga, R., Venegas, P., Guerediaga, J., and Vega, L. F. (2017). Highly accurate geometric calibration for infrared cameras using inexpensive calibration targets. ResearchGate. 5

Vasileska, E. et al. (2020a). Design and implementation of a multisensor coaxial monitoring system for additive manufacturing. *Journal of Manufacturing Science and Engineering*, 140(4):041003. 6

Vasileska, E. et al. (2020b). Layer-wise control of selective laser melting by means of inline melt pool area measurements. *Journal of Laser Applications*, 32(2):n. pag. 6

Wang, W., Ning, J., and Liang, S. (2021). Prediction of lack-of-fusion porosity in laser powder-bed fusion considering boundary conditions and sensitivity to laser power absorption. *International Journal of Advanced Manufacturing Technology*, 112:61–70. 4

Williams, R. et al. (2019). In situ thermography for l-pbf: Effects of layer temperature on porosity, microstructure and mechanical properties. *Additive Manufacturing*, 30:100848. 4

Xiao, L., Lu, M., and Huang, H. (2020). Detection of powder bed defects in selective laser sintering using convolutional neural network. *The International Journal of Advanced Manufacturing Technology*, 107(5):2485–2496. 3

Yakout, M., Phillips, I., Elbestawi, M., and Fang, Q. (2021). In-situ monitoring and detection of spatter agglomeration and delamination during laser-based powder bed fusion of invar 36. *Optics & Laser Technology*, 136:106741. 9

Yang, D., Li, H., Liu, S., Song, C., Yang, Y., Shen, S., Lu, J., Liu, Z., and Zhu, Y. (2020). In situ capture of spatter signature of slm process using maximum entropy double threshold image processing method based on genetic algorithm. *Optics & Laser Technology*, 131:106371. 6

Yoder, S., Nandwana, P., Paquit, V., Kirka, M., Scopel, A., Dehoff, R., and Babu, S. (2019). Approach to qualification using e-pbf in-situ process monitoring in ti-6al-4v. *Additive Manufacturing*, 28:98–106. 3

Appendix A

Farsoon FS271M Nominal Settings

The following are the nominal settings used for the Farsoon FS271M

- Contour Count: 1
- Contour Partition On/Off: 0
- Contour Upskin Speed: 500 mm/s
- Contour Upskin Speed Power 1: 140 W
- Contour Upskin Speed Power 2: 140 W
- Contour Upskin Speed Power 3: 140 W
- Contour Upskin Speed Power 4: 140 W
- Contour Downskin Speed: 800 mm/s
- Contour Downskin Speed Power 1: 140 W
- Contour Downskin Speed Power 2: 140 W
- Contour Downskin Speed Power 3: 140 W
- Contour Downskin Speed Power 4: 140 W

- Contour STD Speed: 700 mm/s
- Contour STD Speed Power 1: 110 W
- Contour STD Speed Power 2: 110 W
- Contour STD Speed Power 3: 110 W
- Contour STD Speed Power 4: 110 W
- Fill Scan Count: 1
- Fill Laser Power: 225 W
- Fill Speed: 1000 mm/s
- Fill Distance: 0.0900 mm
- Fill Initial Angle: 30
- Fill Rotate Angle: 67
- Partition On/Off: 1.00
- Stripe Width: 10.000 mm
- Stripe Overlap: 0.0700 mm
- Stripe Fill Distance: 0.0900 mm
- Stripe Offset: 0.1800 mm
- Checker Start Height: 0 mm
- Checker End Height: 0 mm
- Checker Width X: 10.000 mm
- Checker Width Y: 10.000 mm

- Checker Overlap: 0.0900 mm
- Checker Overlap Line Count: 3
- Checker Border Offset X: 3.00 mm
- Checker Border Offset Y: 3.00 mm
- Checker Border Overlap: 0.0500 mm
- Check Fill Distance: 0.0900 mm
- Checker Skip Layer: 0
- Base Fill Cross: 1.0
- Upper Surface Fill Count: 2
- Upper Surface Laser Power: 225 W
- Upper Surface Speed: 800 mm/s
- Upper Surface Fill Distance: 0.0900 mm
- Down Surface Count: 2
- Down Surface Fill Count: 1
- Down Surface Laser Power: 160 W
- Down Surface Speed: 2000 mm/s
- Down Surface Fill Distance: 0.0600 mm
- Down/Upper Surface Overlap: 0.0500 mm
- Down/Upper Surface Min Length: 0.0500 mm
- Support Scan Count: 0.5

- Support Laser Power: 160 W
- Support Speed: 900 mm/s

Vita

Brett Brady grew up in western Pennsylvania. He attended the United States Naval Academy, where he earned a commission in the United States Navy and a Bachelor of Science in Aerospace Engineering. Selected to attend graduate school through the Officer Scholarship Program, he chose to pursue a Master's in Aerospace Engineering at the University of Tennessee, Knoxville. After graduation, he will relocate to Pensacola, Florida to begin flight school for the United States Navy. He is grateful for all of the support from his family, his team, and his research group.